Vibration of cracked functionally graded microplates by the strain gradient theory and extended isogeometric analysis

Hoang X. Nguyen[a], Elena Atroshchenko[b], Tuan Ngo[c], H. Nguyen-Xuan[d,e], Thuc P. Vo[a,*]

[a]*Department of Mechanical and Construction Engineering, Northumbria University, Newcastle upon Tyne NE1 8ST, United Kingdom*
[b]*Department of Mechanical Engineering, University of Chile, Santiago 8370448, Chile*
[c]*Department of Infrastructure Engineering, The University of Melbourne, Melbourne, Australia*
[d]*CIRTECH Institute, Ho Chi Minh City University of Technology (HUTECH), Ho Chi Minh City, Vietnam*
[e]*Department of Architectural Engineering, Sejong University, 98 Gunja-dong, Gwangjin-gu, Seoul 143-747, South Korea*

Abstract

In this study, the vibration behaviours of functionally graded microplates with cracks are investigated by means of a simple yet rigorous version of Mindlin's generialised continuum and the extended isogeometric analysis (XIGA). The simplified strain gradient theory which includes one material length parameter and an additional *micro-inertia* term is employed to capture the size effects. Meanwhile, the displacement field of the plates is described using the refined plate theory with four unknowns and the XIGA in which enrichment functions are involved to effectively predict the responses of microplates with cracks. In addition, the IGA approach with highly smooth basis functions of non-uniform rational B-spline (NURBS) ensures a clean and efficient treatment of higher continuity requirements in the strain gradient theory. The benchmark numerical results show significant departure from those analysed by the classical continuum elasticity. Indeed, they reveal strong influences of microstructural characteristics on the vibration responses of microplates which are not shown in the platform of the classical theory and the influences are more pronounced as the size of the plates becomes comparable with the material length parameter.

Keywords: Strain gradient theory, Extended isogeometric analysis, Vibration analysis, Functionally graded microplates

1. Introduction

It is well known that the classical continuum theories are size independent meaning and therefore they are unable to capture the small-scale effects. Those effects have been experimentally observed in settings where the sizes of the structure of interest are comparable

*Corresponding author
Email address: thuc.vo@northumbria.ac.uk (Thuc P. Vo)

to material's microstructure lengths [1, 2]. This inability to capture the size effect is attributed to the absence of an internal length scale from the constitutive relation and the local characterisation of stress in the classical theories. The microstructural effects become significantly dominant in structures with very small dimensions which have been used in microelectronmechanical (MEMS) and nanoelectromechanical (NEMS) systems. Meanwhile, the generealised or higher-order continuum theories are equipped with the additional material lengths so that the small-scale effects can be captured efficiently. The theories that are able to account for the size effects include gradient theory by Mindlin [3], micropolar or Cosserat theory [4], couple stress theory by Toupin [5] and Koiter [6].

It is worth mentioning that since the gradient theory includes rotation and stretch gradients, it is more general than the couple stress one which is only based on the constrained rotation. Besides, the gradient theory and Cosserat theory are not similar due to the fact that the latter considers independent rotation components in addition to the displacement components which are used in the former [7]. There are many works have been done based on the couple stress theory [8–10] and Cosserat theory [11–13] to predict the behaviours of small-scale structures. Meanwhile, the generalised strain gradient theory by Mindlin which is also called, for the lowest-order theory, *dipolar gradient theory* or *grade-two theory* is considered as one of the most effective theory. The fundamental idea of this theory is to incorporate an internal displacement field to each particle of a continuum, i.e. the material particle is considered as a deformable medium. According to this theory, the gradients of strain are included in the strain energy density which implies the appearance of new material constants, in addition to two classical Lamé's constants (λ, μ), and the material characteristic lengths. On the other hand, the expression of the kinetic energy density depends upon the *micro-inertia* term leading to the presence of the intrinsic material length that associated with the material microstructure. It is worth commenting that, at the early stage of the development, the gradient theories were highly complex with many independent parameters which discouraged researchers and engineers to consider them seriously for mechanics problems. Later, the theories were simplified and only one parameter in addition to the Lamé constants is involved. The comprehensive reviews on the development of the gradient theories can be found in the literature [7, 14, 15]. The gradient theories, both the general and the simplified ones, have been widely applied in many problem including stress concentration [16, 17], wave propagation [18, 19], plasticity [20, 21], fracture [22, 23] and static analysis [24].

In the context of plate theories, there is a great deal of works devoted to the development of reliable mathematical models that govern their behaviours. It is started with the classical plate theory or usually called the Kirchhoff-Love plate theory in which three degrees of freedom corresponding to displacements are involved. The fundamental idea of this theory is to neglect the shear deformations by assuming that the cross sections normal to the midplane remain normal during deformations. This theory appears to be simple and effective when dealing with thin plates with large length-to-thickness ratios where the transverse shear stresses and strains are negligibly small. However, classical plate theory shows its drawbacks in the analysis of thick plates in which the transverse shear components are significant. In order to overcome these shortcomings, the first-order shear deformation

theory which is also known as Reissner-Mindlin plate theory is proposed acknowledging the existence of the shear deformations. Consequently, this theory with five unknowns (three displacements and two rotations) is capable of reliably predicting the structural behaviours of both thin and thick plates. However, the major issue of the theory is the necessity to calculate the shear correction factor to match the numerical results with the analytical ones. The procedure to determine this factor may not be able to be established due to the fact that it is problem dependent. Several higher-order plate theories have been proposed to eliminate this factor. Reddy [25] pioneered the use of the five-unknown third-order plate theory which incorporates shear deformations without using the shear correction factor. In an effort to simplify yet maintain all beneficial features of Reddy's theory, Senthilnathan [26] deliberately split the transverse displacement into bending and shearing parts and employed their spatial derivatives to represent rotations. He derived the so-called refined plate theory (RPT) with four degrees of freedom. Recently, Karttunen et al. [27] worked on an approach that linked plate theories and elasticity solutions in which the exact 3D plate solution and the results for interior plate problem were presented. There is a great deal of studies that utilised the plate theories to estimate the structural responses of structures [28–30].

The attention to the combination of the plate theories and generalised continuum theories including their variations to investigate the behaviours of small-scale plates has been constantly increased over the last few years. Papargyri-Beskou and Beskos [24] conducted static, stability and dynamic analysis of Kirchhoff plates using the strain gradient theory (SGT) with one additional material constant. Zhang et al. [31] utilised the Fourier series to predict the mechanical behaviours of small-scale plate based on Kirchhoff theory. Farzam Dadgar-Rad [32] analysed the strain gradient Reissner-Mindlin plate using C^0 quadrilateral elements. Ji et al. [33] proposed a comparison of strain gradient theories which were used in the analysis of functionally graded (FG) circular plates. Khakalo and Niiranen [34, 35] employed the SGT for the analysis of micro/nano materials and structures as well as stress analysis around cylindrical holes with bi-axial tension. However, in most of the works, the micro-inertia term which appears in the kinetic energy density of the original SGT has been ignored. In addition, the solution procedures involve either analytical approach for limited study or finite element analysis with less requirement on the continuity of the inter-elements. It is worth noting that when a plate theory is combined with the SGT, the resulting equation are of sixth-order leading to third-order derivatives in the weak form, which requires at least C^2-continuity of the basis functions. Such higher order requirements can be efficiently handled by the isogeometric analysis (IGA) approach.

The IGA which is introduced by Hughes et al. [36] is capable of handling the high continuity requirements easily with appropriate basis functions. This newly developed method also aims at the integration of the design and analysis in industrial processes. This fundamental idea is fulfilled by employing the same basis functions to represent the geometries and to approximate the solution fields. Among the possibilities, the non-uniform rational B-splines (NURBS) is the most popular option of a basis function as it has a dominant establishment in the Computer Aided Design (CAD) industry. While NURBS can exactly represent complex geometries, the basis function is also able to approximate the unknowns with higher order of continuity effectively since it is highly smooth. Owing to this strik-

ing feature, NURBS can easily handle the sixth-order plate problems based on higher-order plate theory and generalised continuum theory where C^2 continuity is required. The self-contained reviews on the IGA can be found in a number of works in the literature [37–40]. IGA has found its application in broad fields of solid mechanics including those with small-scale structures using beam/plate theories and generalised continuum theories and their variants [41–46]. In attempts to deal with structural fractures, the ideas of extended finite element method (XFEM) [47] are incorporated in the platform of the IGA. While Benson et al. [48] presented the application of XIGA in dealing with the fracture mechanic problems, De Luycker et al. [49] showed the results of XIGA for linear fracture mechanics with good accuracy and better convergence rate. Ghorashi et al. [50] utilised the XIGA for the simulation of stationary and propagating cracks.

Regarding the investigation into plates with cracks, there is a well established body of work on the mechanical behaviours of such structures. Stahl and Keer [51] studied the vibration and buckling responses of cracked rectangular plates in which the dual series equations and the homogeneous Fredholm integral equations were considered. Bachene et al. [52] and Natarajan et al. [53] applied the XFEM to model the discontinuities and solve for the vibration responses of cracked plates. Tran et al. [54] analysed the vibrations of FG plates with cracks by means of the XIGA. However, most of the research dealt with normal-size plates using classical continuum theories without considering size effects. Recently, Liu et al. [55] studied the size-dependent effects of cracked plates based on Reissner-Mindlin plate theory and modified couple stress theory. However, as mentioned above, these theories have their own shortcomings in terms of choosing shear correction factor and accounting for the micro-inertia term.

In this study, in order to fill the existing gaps and enrich the research into small-scale plates with cracks, the vibration analysis of cracked FG microplates by means of the SGT and XIGA will be presented. While the simplified SGT with one internal length scale incorporating micro-inertia term is employed to efficiently capture the size-dependent effects, the displacement field of the plates is modelled by the RPT. In the combination of these particular continuum theory and plate theory, the sixth-order governing equations will be formed. Consequently, elements with C^2-continuities are required to be able to numerically solve the equations. This condition is effectively fulfilled in the platform of the NURBS-based XIGA in which Heaviside and novel enrichment functions are employed to model the discontinuities along the crack path and capture the near tip asymptotic field.

The outline of this study is as follows. Whereas Section 2 gives a brief review on the SGT and kinematics of plates, Section 3 provides the formulation of the XIGA and the discretisation procedure. Section 4 presents the convergence study and numerical results of cracked plates with various shapes, crack locations, and boundary conditions, as well as the effects of the scale parameters on the vibration responses. The study is closed with concluding remarks which are given in Section 5.

2. Strain gradient FG plate formulation

2.1. Brief review of the strain gradient theory (SGT)

The general SGT with microstructure is initially presented in the benchmark paper of Mindlin [3]. In the most general case, the strain energy density and the kinetic energy density are both formulated in terms of quantities on the microscale and on the macroscale. However, the formulations require in total of eighteen constitutive coefficients. Consequently, experimental identification of those constants is extremely difficult which seriously limits the use of this theory in practical analysis and design. Fortunately, by making a number of assumptions, Mindlin proposed simpler versions of the gradient elasticity theory with less number of constants which allows the strain energy density to be dependent upon the macroscopic displacement only. The simpler versions can be categorised into three forms based on how the microscopic deformation gradient κ_{ijk} and the macroscopic displacement u_i related. While the microscopic deformation gradient is expressed directly in terms of the second gradient of the macroscopic displacement in Form I, $\kappa_{ijk} = u_{k,ij}$, it is defined as the first gradient of the macroscopic strain in Form II, $\kappa_{ijk} = \varepsilon_{jk,i}$. It is worth commenting that, according to the classical continuum, the macroscopic strain is defined as the first gradient of the macroscopic displacement. In Form III, the microscopic deformations are split into the gradient of macroscopic rotation, $\chi_{ij} = \frac{1}{2} e_{jlm} u_{m,il}$, and the symmetric part of the second gradient of macroscopic displacement, $\kappa_{ijk} = \frac{1}{3}\left(u_{i,jk} + u_{j,ik} + u_{k,ij}\right)$ [14].

In this study, a simplified version of the SGT derived from the Form II will be used. As a starting point, the strain energy density is expressed with seven material constants including two Lamé's constants (λ, μ) as follows [3, 18]

$$U_0\left(\varepsilon, \kappa\right) = \frac{1}{2}\lambda\varepsilon_{ii}\varepsilon_{jj} + \mu\varepsilon_{ij}\varepsilon_{ij} + a_1\kappa_{iik}\kappa_{kjj} + a_2\kappa_{kii}\kappa_{kjj} + a_3\kappa_{iij}\kappa_{jjk} + a_4\kappa_{kij}\kappa_{kij} + a_5\kappa_{kij}\kappa_{jik}, \quad (1)$$

where the Latin indices span the range $(1, 2, 3)$ and the classical strain tensor is defined as the first gradient of the macroscopic displacement

$$\varepsilon_{ij} = \frac{1}{2}\left(u_{j,i} + u_{i,j}\right) = \varepsilon_{ji}, \quad (2)$$

and the microscopic deformation gradient or also called the strain gradient tensor are expressed in terms of the first gradient of the macroscopic strain, in turns, the second gradient of the displacement as follows

$$\kappa_{ijk} = \varepsilon_{jk,i} = \frac{1}{2}\left(u_{k,ji} + u_{j,ki}\right) = \kappa_{ikj}. \quad (3)$$

By making further assumptions [15], $a_2 = \frac{1}{2}\lambda\ell^2, a_4 = \mu\ell^2, a_1 = a_3 = a_5 = 0$, where ℓ is the characteristic length or material length scale parameter and ℓ^2 represents the volumetric strain energy gradient, the strain energy density can be expressed with only one additional constant

$$U_0 = \frac{1}{2}\lambda\varepsilon_{ii}\varepsilon_{jj} + \mu\varepsilon_{ij}\varepsilon_{ij} + \ell^2\left(\frac{1}{2}\lambda\varepsilon_{ii,k}\varepsilon_{jj,k} + \mu\varepsilon_{ij,k}\varepsilon_{ij,k}\right). \quad (4)$$

Meanwhile, the kinetic energy density in Cartesian coordinate system is given as follows

$$K_0 = \frac{1}{2}\rho \dot{u}_i \dot{u}_i + \frac{1}{6}\rho d^2 \frac{\partial \dot{u}_j}{\partial x_i}\frac{\partial \dot{u}_j}{\partial x_i} \tag{5}$$

where ρ is the mass density, the time derivative is represented by the superposed dot, and $2d$ is the size of the cube edges of the unit cell [18]. In their study on dispersive Rayleigh-wave propagation, Georgiadis et al. [15] suggested the relation between the material length scale and the size of the cube edges to be $\ell^2 = (0.1d)^2$. The second term of the right-hand-side (RHS) of Eq. (5) which is ignored in classical theory represents the micro-inertia of the continuum. This velocity gradient involvement allows the SGT to have a more detailed description of the motion which is used to analyse the vibration of the small-scale structures.

2.2. Kinematics of the refined plate theory (RPT)

Senthilnathan et al. [26] proposed the RPT with four unknowns in which the displacement field is given as follows

$$u(x,y,z) = u_0(x,y) - z w_{b,x}(x,y) + g(z)\, w_{s,x}(x,y), \tag{6a}$$
$$v(x,y,z) = v_0(x,y) - z w_{b,y}(x,y) + g(z)\, w_{s,y}(x,y), \tag{6b}$$
$$w(x,y,z) = w_b(x,y) + w_s(x,y), \tag{6c}$$

where u_0 and v_0 are in-plane displacement components of a material point and w_b and w_s denote the bending and shear components of transverse displacement, respectively. The distribution of transverse strains and stresses through the thickness is represented by the function g in which $g : z \mapsto g(z) = f(z) - z$. The function f is chosen so that its first derivative with respect to z is identically zero at the top and bottom surfaces ($z = \pm h/2$) [41].

From Eq. (2), the displacement-strain relations associated with the RPT can be explicitly presented as follows

$$\boldsymbol{\varepsilon} = \boldsymbol{\varepsilon}_0 + z\boldsymbol{\kappa}_b + g(z)\,\boldsymbol{\kappa}_s, \tag{7a}$$
$$\boldsymbol{\gamma} = [1 + g'(z)]\,\boldsymbol{\varepsilon}_s = f'(z)\,\boldsymbol{\varepsilon}_s, \tag{7b}$$

where

$$\boldsymbol{\varepsilon} = \begin{bmatrix} \varepsilon_x & \varepsilon_y & \gamma_{xy} \end{bmatrix}^T, \tag{8a}$$
$$\boldsymbol{\gamma} = \begin{bmatrix} \gamma_{xz} & \gamma_{yz} \end{bmatrix}^T, \tag{8b}$$

and the in-plane, bending and shear strains are expressed as

$$\boldsymbol{\varepsilon}_0 = \begin{bmatrix} u_{0,x} \\ v_{0,y} \\ u_{0,y} + v_{0,x} \end{bmatrix}, \quad \boldsymbol{\kappa}_b = -\begin{bmatrix} w_{b,xx} \\ w_{b,yy} \\ 2w_{b,xy} \end{bmatrix}, \quad \boldsymbol{\kappa}_s = \begin{bmatrix} w_{s,xx} \\ w_{s,yy} \\ 2w_{s,xy} \end{bmatrix}, \quad \boldsymbol{\varepsilon}_s = \begin{bmatrix} w_{s,x} \\ w_{s,y} \end{bmatrix}. \tag{9}$$

By using Eqs. (3) and (7), the strain gradient components can be given in a set of three equations as follows

$$\boldsymbol{\kappa}_i = \boldsymbol{\kappa}_i^0 + z\boldsymbol{\kappa}_i^1 + g\left(z\right)\boldsymbol{\kappa}_i^2 + g'\left(z\right)\boldsymbol{\kappa}_i^3 + g''\left(z\right)\boldsymbol{\kappa}_i^4, \tag{10}$$

where i represents three possibilities of $\{x, y, z\}$. The detailed expressions of the strain gradient tensors in terms of macroscopic displacement components can be found in Appendix A.

2.3. Constitutive relations

In view of Eq. (4), the constitutive equation in the classical elasticity theory can be determined as follows

$$\sigma_{ij} = \frac{\partial U_0}{\partial \varepsilon_{ij}} = \lambda\delta_{ij}\varepsilon_{kk} + 2\mu\varepsilon_{ij}, \tag{11}$$

where $\sigma_{ij} = \sigma_{ji}$ are components of monopolar (or Cauchy) stress tensor. Meanwhile, the strain gradient constitutive equations are calculated as

$$\eta_{ijk} = \frac{\partial U_0}{\partial \kappa_{ijk}} = \ell^2\left(\lambda\delta_{jk}\kappa_{ipp} + 2\mu\kappa_{ijk}\right) = \ell^2\left(\lambda\delta_{jk}\varepsilon_{pp,i} + 2\mu\varepsilon_{jk,i}\right), \tag{12}$$

in which $\eta_{ijk} = \eta_{ikj}$ denote components of dipolar (or double) stress tensor having dimension of [force][length]$^{-1}$. The Lamé's constants λ and μ, which is also known as shear modulus G, are related to the effective Young's modulus E and Poisson's ratio ν as follows

$$\lambda = \frac{\nu E}{\left(1+\nu\right)\left(1-2\nu\right)}, \tag{13a}$$

$$\mu = \frac{E}{2\left(1+\nu\right)}. \tag{13b}$$

It should be noted that the effective engineering constants E and ν for the FGMs which is used in this study are varied continuously through the structure's thickness. The estimation of these constants at a specific point can be done following the rules of mixture or the Mori-Tanaka scheme [56, 57]. A review of these estimating models and the properties of the FGMs can be found in one of the authors' published works [41]. Within the scope of this study, for the sake of simplicity, the rule of mixture is employed to determine the effective Young's modulus E and Poisson's ratio ν following these equations

$$E_e(z) = E_m V_m(z) + E_c V_c(z), \tag{14a}$$

$$\nu_e(z) = \nu_m V_m(z) + \nu_c V_c(z), \tag{14b}$$

where the volume fractions V_c and V_m of the ceramic and metal phases, respectively, which are two constituents in the mixture of the FGMs, through the plate's thickness h are given by

$$V_c\left(z\right) = \left(\frac{1}{2} + \frac{z}{h}\right)^n, \quad V_m = 1 - V_c, \quad -\frac{h}{2} \le z \le \frac{h}{2}, \tag{15}$$

in which n is the material index indicating the profile of material variation through the thickness. As can be interpreted from Eq. (15), this estimation enables the materials to change smoothly from metal at the bottom surface to ceramic at the top. In addition, the mixture becomes fully homogeneous ceramic material if $n = 0$ while fully homogeneous metal material is obtained as n goes toward $+\infty$.

With the assumption of $\sigma_{zz} = 0$, the monopolar stress components can be written explicitly as follows

$$\begin{Bmatrix} \sigma_x \\ \sigma_y \\ \sigma_{xy} \\ \sigma_{xz} \\ \sigma_{yz} \end{Bmatrix} = \begin{bmatrix} Q_{11} & Q_{12} & 0 & 0 & 0 \\ Q_{21} & Q_{22} & 0 & 0 & 0 \\ 0 & 0 & Q_{66} & 0 & 0 \\ 0 & 0 & 0 & Q_{55} & 0 \\ 0 & 0 & 0 & 0 & Q_{44} \end{bmatrix} \begin{Bmatrix} \varepsilon_x \\ \varepsilon_y \\ \gamma_{xy} \\ \gamma_{xz} \\ \gamma_{yz} \end{Bmatrix} \tag{16}$$

where

$$Q_{11} = Q_{22} = \frac{E}{1-\nu^2};\;\; Q_{12} = Q_{21} = \frac{\nu E}{1-\nu^2};\;\; Q_{44} = Q_{55} = Q_{66} = \frac{E}{2\left(1+\nu\right)} \tag{17}$$

Meanwhile, the dipolar stress components are expressed in a set of three equations as follows

$$\begin{Bmatrix} \eta_{ixx} \\ \eta_{iyy} \\ \eta_{iyz} \\ \eta_{ixz} \\ \eta_{ixy} \end{Bmatrix} = \ell^2 \begin{bmatrix} Q_{11} & Q_{12} & 0 & 0 & 0 \\ Q_{21} & Q_{22} & 0 & 0 & 0 \\ 0 & 0 & Q_{44} & 0 & 0 \\ 0 & 0 & 0 & Q_{55} & 0 \\ 0 & 0 & 0 & 0 & Q_{66} \end{bmatrix} \begin{Bmatrix} \kappa_{ixx} \\ \kappa_{iyy} \\ 2\kappa_{iyz} \\ 2\kappa_{ixz} \\ 2\kappa_{ixy} \end{Bmatrix} \tag{18}$$

where i is one of the values from the set $\{x, y, z\}$.

2.4. Variational formulation

In view of Eqs. (4) and (5), the strain energy and kinetic energy can be calculated by taking the integration of the energy densities over the volume occupied by the structures as follows

$$U = \int_V U_0 dV = \int_V \boldsymbol{\sigma} : \boldsymbol{\epsilon} dV + \int_V \boldsymbol{\eta} : \boldsymbol{\kappa} dV \tag{19a}$$

$$K = \int_V K_0 dV = \int_V \left(\frac{1}{2}\rho \dot{\mathbf{u}} \cdot \dot{\mathbf{u}} + \frac{1}{6}\rho d^2 \frac{\partial \dot{\mathbf{u}}}{\partial \mathbf{x}} \cdot \frac{\partial \dot{\mathbf{u}}}{\partial \mathbf{x}} \right) dV, \tag{19b}$$

where $\boldsymbol{\sigma}$, $\boldsymbol{\epsilon}$, $\boldsymbol{\eta}$, and $\boldsymbol{\kappa}$ represent monopolar stress, strain, dipolar stress, and strain gradient components, respectively. Meanwhile, $\mathbf{u} = \{u, v, w\}^T$ and $\mathbf{x}$ are displacement and three-dimensional spatial components, and V is the region in $\mathbb{R}^3$ occupied by the body. As can be observed from Eq. (19), both strain energy and kinetic energy consist of the classical terms and gradient terms. This inclusion enables the current approach to be able to comprehensively describe the structural behaviours across the scales.

By applying the principle of virtual work, the weak form of the free vibration problem can be expressed as follows

$$\left(\int_{\Omega}\delta\boldsymbol{\varepsilon}_b^T\mathbf{D}^b\boldsymbol{\varepsilon}_b d\Omega+\int_{\Omega}\delta\boldsymbol{\varepsilon}_s^T\mathbf{D}^s\boldsymbol{\varepsilon}_s d\Omega\right)+\left(\int_{\Omega}\delta\hat{\boldsymbol{\kappa}}_x^T\hat{\mathbf{D}}\hat{\boldsymbol{\kappa}}_x d\Omega+\int_{\Omega}\delta\hat{\boldsymbol{\kappa}}_y^T\hat{\mathbf{D}}\hat{\boldsymbol{\kappa}}_y d\Omega+\int_{\Omega}\delta\hat{\boldsymbol{\kappa}}_z^T\hat{\mathbf{D}}\hat{\boldsymbol{\kappa}}_z d\Omega\right)$$
$$=\int_{\Omega}\delta\tilde{\mathbf{u}}^T\tilde{\mathbf{m}}\ddot{\tilde{\mathbf{u}}}d\Omega+\frac{1}{3}d^2\int_{\Omega}\left(\delta\tilde{\mathbf{u}}_{,x}^T\tilde{\mathbf{m}}\ddot{\tilde{\mathbf{u}}}_{,x}+\delta\tilde{\mathbf{u}}_{,y}^T\tilde{\mathbf{m}}\ddot{\tilde{\mathbf{u}}}_{,y}+\delta\tilde{\mathbf{u}}_{,z}^T\tilde{\mathbf{m}}\ddot{\tilde{\mathbf{u}}}_{,z}\right)d\Omega \tag{20}$$

where Ω is the domain in $\mathbb{R}^2$ occupied by the mid-plane of the plate ($V=\Omega\times\left[-\frac{h}{2},\frac{h}{2}\right]$) and the strain tensor as well as the material matrix are

$$\boldsymbol{\varepsilon}_b=\left\{\begin{array}{c}\boldsymbol{\varepsilon}_0\\ \boldsymbol{\kappa}_b\\ \boldsymbol{\kappa}_s\end{array}\right\},\quad \mathbf{D}^b=\left[\begin{array}{ccc}\mathbf{A}&\mathbf{B}&\mathbf{E}\\ \mathbf{B}&\mathbf{D}&\mathbf{F}\\ \mathbf{E}&\mathbf{F}&\mathbf{H}\end{array}\right], \tag{21}$$

in which matrix components are defined as

$$(A_{ij},B_{ij},D_{ij},E_{ij},F_{ij},H_{ij})=\int_{-h/2}^{h/2}\left(1,z,z^2,g,zg,g^2\right)\bar{Q}_{ij}dz, \tag{22a}$$

$$D_{ij}^s=\int_{-h/2}^{h/2}\left[1+g'(z)\right]^2\hat{Q}_{ij}dz, \tag{22b}$$

$$\bar{\mathbf{Q}}=\left[\begin{array}{ccc}Q_{11}&Q_{12}&0\\ Q_{21}&Q_{22}&0\\ 0&0&Q_{66}\end{array}\right], \tag{22c}$$

$$\hat{\mathbf{Q}}=\left[\begin{array}{cc}Q_{44}&0\\ 0&Q_{55}\end{array}\right]. \tag{22d}$$

Meanwhile, the strain gradient tensor and the material matrices related to gradient terms are

$$\hat{\boldsymbol{\kappa}}_x=\left\{\begin{array}{c}\boldsymbol{\kappa}_x^0\\ \boldsymbol{\kappa}_x^1\\ \boldsymbol{\kappa}_x^2\\ \boldsymbol{\kappa}_x^3\\ \boldsymbol{\kappa}_x^4\end{array}\right\},\quad \hat{\boldsymbol{\kappa}}_y=\left\{\begin{array}{c}\boldsymbol{\kappa}_y^0\\ \boldsymbol{\kappa}_y^1\\ \boldsymbol{\kappa}_y^2\\ \boldsymbol{\kappa}_y^3\\ \boldsymbol{\kappa}_y^4\end{array}\right\},\quad \hat{\boldsymbol{\kappa}}_z=\left\{\begin{array}{c}\boldsymbol{\kappa}_z^0\\ \boldsymbol{\kappa}_z^1\\ \boldsymbol{\kappa}_z^2\\ \boldsymbol{\kappa}_z^3\\ \boldsymbol{\kappa}_z^4\end{array}\right\},\quad \hat{\mathbf{D}}=\left[\begin{array}{ccccc}\mathbf{A}^g&\mathbf{B}^g&\mathbf{E}^g&\mathbf{G}^g&\mathbf{M}^g\\ \mathbf{B}^g&\mathbf{D}^g&\mathbf{F}^g&\mathbf{I}^g&\mathbf{N}^g\\ \mathbf{E}^g&\mathbf{F}^g&\mathbf{H}^g&\mathbf{J}^g&\mathbf{P}^g\\ \mathbf{G}^g&\mathbf{I}^g&\mathbf{J}^g&\mathbf{L}^g&\mathbf{Q}^g\\ \mathbf{M}^g&\mathbf{N}^g&\mathbf{P}^g&\mathbf{Q}^g&\mathbf{R}^g\end{array}\right], \tag{23}$$

in which

$$\left(A_{ij}^g,B_{ij}^g,D_{ij}^g,E_{ij}^g,F_{ij}^g,H_{ij}^g,G_{ij}^g,I_{ij}^g,J_{ij}^g,L_{ij}^g,M_{ij}^g,N_{ij}^g,P_{ij}^g,Q_{ij}^g,R_{ij}^g\right)$$
$$=\int_{-h/2}^{h/2}\left(1,z,z^2,g,zg,g^2,g',zg',gg',(g')^2,g'',zg'',gg'',g'g'',(g'')^2\right)Q_{ij}dz. \tag{24}$$

For the terms related to the kinetic energy,

$$\tilde{\mathbf{u}} = \left\{ \begin{array}{cccccccccc} u_0 & -w_{b,x} & w_{s,x} & v_0 & -w_{b,y} & w_{s,y} & w_b & w_s & 0 \end{array} \right\}^T, \quad \tilde{\mathbf{m}} = \left[\begin{array}{ccc} \mathbf{I}_0 & 0 & 0 \\ 0 & \mathbf{I}_0 & 0 \\ 0 & 0 & \mathbf{I}_1 \end{array} \right], \tag{25}$$

where

$$\mathbf{I}_0 = \left[\begin{array}{ccc} I_1 & I_2 & I_4 \\ I_2 & I_3 & I_5 \\ I_4 & I_5 & I_6 \end{array} \right], \ \mathbf{I}_1 = \left[\begin{array}{ccc} I_1 & I_1 & 0 \\ I_1 & I_1 & 0 \\ 0 & 0 & 0 \end{array} \right], \tag{26a}$$

$$(I_1, I_2, I_3, I_4, I_5, I_6) = \int_{-h/2}^{h/2} \rho \left(1, z, z^2, g, zg, g^2\right) dz. \tag{26b}$$

It is worth noting that even though they are appeared in Eq. (20) for the general cases, in this study, the components related to the derivatives of $\tilde{\mathbf{u}}$ with respect to z are identically zero.

3. Extended isogeometric analysis (XIGA) discretisation for microplate with cracks

In standard IGA, in order to calculate the basis functions, the ideas of knot vector were introduced first. It is non-decreasing vector $\Xi = \{\xi_1, \xi_2, \ldots, \xi_{n+p+1}\}$ where ith knot $\xi_i \in \mathbb{R}$, n and p are the number of basis functions and the polynomial order, respectively. Having the knot vectors defined, the B-spline and NURBS basis functions can be computed. For the sake of brevity, the explicit derivations of those functions, which can readily find in the literature [36, 58], are not presented here.

In the platform of the XIGA, the displacements of a plate with cracks are predicted by enriching the standard approximation as follows

$$\mathbf{u}^h(\mathbf{x}) = \sum_{I \in \mathcal{N}} R_I(\mathbf{x})\, \mathbf{q}_I + \sum_{J \in \mathcal{N}_{cr}} R_J(\mathbf{x}) \left(H(\mathbf{x}) - H(\mathbf{x}_J)\right) \mathbf{a}_J + \sum_{K \in \mathcal{N}_{tip}} R_K(\mathbf{x}) \sum_{\alpha=1}^{n_\alpha} \left(B_\alpha(\mathbf{x}) - B_\alpha(\mathbf{x}_K)\right) \mathbf{b}_{\alpha K}, \tag{27}$$

where the R_I, R_J, and R_K are NURBS basis functions, $H(\mathbf{x})$ and $B_\alpha(\mathbf{x})$ are Heaviside and crack-tip enrichment functions, respectively. While $\mathbf{q}_I$, $\mathbf{a}_J$, and $\mathbf{b}_{\alpha K}$ are variables associated with the control points and enrichments, n_α represents the number of crack-tip enrichment functions used. Meanwhile, $\mathbf{x}$ is now two-dimensional spatial components. It should be noted that the local enrichment functions R_J and R_K are not necessary to be the same as the shape function R_I which is used for the displacement approximation [59]. $\mathcal{N}$ is the set of all control points. Besides, $\mathcal{N}_{cr}$ represents the set of control points whose supports are bisected by the crack while $\mathcal{N}_{tip}$ is the set of all control points whose support contains the crack tip. As the integration gets less reliable results in the elements being cut by the crack

path or element with crack tip, in this study, the full integration with subtriangle technique is used to improve the approximation in such elements. A brief description of different sets of control point and how enriched elements being segmented into subtriangles is provided in Fig. 1.

The Heaviside function which is employed to model the discontinuity in structure with cracks takes values of $+1$ if the point of interest in physical coordinate $\mathbf{x}$ is on one side the crack and -1 otherwise. Giving $\mathbf{x}^*$ is the closest point on the crack to $\mathbf{x}$ and $\mathbf{e}_n$ is the unit normal vector at $\mathbf{x}^*$, the function can be expressed mathematically as follows [47]

$$H\left(\mathbf{x}\right)=\begin{cases}+1 & \text{if } (\mathbf{x}-\mathbf{x}^*).\mathbf{e}_n>0,\\ -1 & \text{otherwise.}\end{cases} \tag{28}$$

Fig. 2 illustrates a simple representation of the Heaviside function and its effects on the basis functions in approximation of fields in which a crack at $\xi=0.4$ is considered.

Meanwhile, the crack-tip enrichment functions improve the accuracy of the solution by spanning the near tip asymptotic field and reliably describing the singular stress field near the crack tip. The choice of the crack-tip enrichment functions depends on the original displacement description of the problem and how well the function can capture the near tip asymptotic field [47]. In this specific problem of the small-scale plates in which the RPT and SGT are employed, the enrichment functions should also account for the inclusion of high-order strain gradient terms [60]. They are defined in the local polar coordinates associated with the crack tip as follows

$$\mathbf{B}\equiv\begin{cases}\left[r^{3/2}\sin\dfrac{\theta}{2},r^{3/2}\cos\dfrac{\theta}{2},r^{3/2}\sin\dfrac{3\theta}{2},r^{3/2}\cos\dfrac{3\theta}{2},r^{3/2}\sin\dfrac{5\theta}{2},r^{3/2}\cos\dfrac{5\theta}{2}\right] & \text{for } u_0,v_0,\\ \left[r^{3/2}\sin\dfrac{\theta}{2},r^{3/2}\sin\dfrac{3\theta}{2},r^{5/2}\sin\dfrac{\theta}{2},r^{5/2}\cos\dfrac{\theta}{2},r^{5/2}\sin\dfrac{3\theta}{2},r^{5/2}\cos\dfrac{3\theta}{2},r^{5/2}\sin\dfrac{5\theta}{2},r^{5/2}\cos\dfrac{5\theta}{2}\right] & \text{for } w_b,w_s.\end{cases} \tag{29}$$

By substituting the approximation in Eq. (27) into the strains derived in Eqs. (7)-(9), the classical strain components can be expressed in terms of the basis functions and enrichment functions as follows

$$\boldsymbol{\varepsilon}_b=\begin{bmatrix}\boldsymbol{\varepsilon}_0^T & \boldsymbol{\kappa}_b^T & \boldsymbol{\kappa}_s^T\end{bmatrix}^T=\sum_A\begin{bmatrix}\left(\mathbf{B}_A^m\right)^T & \left(\mathbf{B}_A^{b1}\right)^T & \left(\mathbf{B}_A^{b2}\right)^T\end{bmatrix}^T\mathbf{q}_A, \tag{30a}$$

$$\boldsymbol{\varepsilon}_s=\sum_A\mathbf{B}_A^s\mathbf{q}_A, \tag{30b}$$

where $\mathbf{q}_A$ consists of both displacement and enrichment variables and the detailed expressions of $\mathbf{B}_A^m,\mathbf{B}_A^{b1},\mathbf{B}_A^{b2}$, and $\mathbf{B}_A^s$ matrices are given in Appendix B.

Similarly, by using Eqs. (27), (10) and Appendix A, the strain gradient tensors can be expressed in the form of the following equations

$$\begin{bmatrix}\left(\boldsymbol{\kappa}_i^0\right)^T & \left(\boldsymbol{\kappa}_i^1\right)^T & \left(\boldsymbol{\kappa}_i^2\right)^T & \left(\boldsymbol{\kappa}_i^3\right)^T & \left(\boldsymbol{\kappa}_i^4\right)^T\end{bmatrix}^T=\sum_A\begin{bmatrix}\left(\mathbf{B}_A^{i0}\right)^T & \left(\mathbf{B}_A^{i1}\right)^T & \left(\mathbf{B}_A^{i2}\right)^T & \left(\mathbf{B}_A^{i3}\right)^T & \left(\mathbf{B}_A^{i4}\right)^T\end{bmatrix}^T\mathbf{q}_A, \tag{31}$$

where i represents three possibilities of $\{x, y, z\}$ and the detailed expressions of the matrices in the RHS are given in Appendix B.

The discretised systems of equations for the free vibration analysis using XIGA is

$$\left(\mathbf{K} - \omega^2 \mathbf{M}\right) \mathbf{q} = \mathbf{0}, \tag{32}$$

where the global stiffness and mass matrices are respectively given as

$$\mathbf{K} = \mathbf{K}_c + \left(\mathbf{K}_{gx} + \mathbf{K}_{gy} + \mathbf{K}_{gz}\right), \tag{33a}$$

$$\mathbf{M} = \mathbf{M}_c + \left(\mathbf{M}_{gx} + \mathbf{M}_{gy} + \mathbf{M}_{gz}\right), \tag{33b}$$

in which the subscript c indicates the matrices on RHS are associated with the classical terms while the remains are with the strain gradient terms. The element stiffness and mass matrices from which the global matrices are assembled are given in Appendix C and Appendix D, respectively. It is worth noting that, as discussed, the derivatives of displacement variables with respect to z are identically zero yielding $\mathbf{M}_{gz}$ to be a zero matrix.

As a final note to close this section, observing from Appendix B, the third derivatives of the approximation functions are required in the extended isogeometric discretisation process which means the C^2-continuity between elements should be maintained. This requirement of highly smooth elements is not fulfilled in the platform of the traditional finite element methods. However, this issue can be addressed naturally and efficiently by using NURBS-based basis functions with polynomial order $p \geq 3$.

4. Numerical results and discussion

In this section, the numerical results of the vibration analysis of small-scale FG plates with cracks will be presented. The microplates are made of $\mathrm{Al}/\mathrm{Al_2O_3}$ in which the material properties are $E_c = 380$ GPa, $E_m = 70$ GPa, $\nu_c = \nu_m = 0.3$, $\rho_c = 3800$ (kg/m^3), $\rho_m = 2707$ (kg/m^3). Unless specifically mentioned, the rule of mixture is employed to describe the distribution of the ceramic and metal phases for numerical analyses in this section. It should be noted that $\ell/h \equiv 0$ implies the analysis is conducted within the context of classical continuum, i.e. no size effects considered. As the formulation of the SGT-based vibration problems requires at least C^2-continuity elements, the quartic basis functions ($p = 4$) which satisfy up to C^3-continuous requirements have been employed. Meanwhile, the boundary conditions are applied using similar techniques that have been discussed in the work of Nguyen et al. [41].

4.1. Convergence and verification

For the illustration of the convergence and validity of the proposed approach, a number of analyses for square plate with different parameters of element meshes have been tested. Since there are no results reported for the vibration of cracked FG microplates based on the SGT, the numerical results are first generated for the plates without the size-dependent effects. Fig. 3 shows the convergence of the fundamental frequency of the simply-supported

Al/Al_2O_3 square plate with a crack in which the frequency normalisation $\bar{\omega} = \omega \frac{a^2}{h}\sqrt{\frac{\rho_c}{E_c}}$ is used. As can be observed, the solutions converge well to the reference 3D elasticity results, which were reported by Huang et al. [61].

Table 1 presents a complete comparison of the results generated from the proposed method and those of other approaches including 3D elasticity and Ritz method by Huang et al. [61], XFEM by Natarajan et al. [53], and XIGA using the third-order shear deformation theory (TSDT) by Tran et al. [54]. As can be seen, for the case of absence of size effects, i.e. $\ell/h \equiv 0$, the present results of the first five natural frequencies of the plates are in good agreement with the existing analytical and approximate solutions in the literature.

In the next parts, investigations into the vibrational behaviours of square, circular, and annular microplates with edge cracks and center cracks will be presented.

4.2. Square microplates with cracks

In this part, a number of numerical studies of vibration responses of square FG microplates with edge and center cracks are presented to demonstrate the effects of material length scale ratio ℓ/h, aspect ratio a/h, and material index n on the natural frequencies of the small-scale structures. The geometry configurations of the square plates with edge and center cracks are given in Fig. 4. In order to present the numerical results efficiently, unless otherwise stated, the normalisation of frequency mentioned in the previous section is used. As there are no results reported for the vibration of cracked microplates using the SGT, the solutions in this study can be used as benchmark references.

Fig. 5 presents the effects of the material length scale ratio ℓ/h on the natural frequencies of SSSS Al/Al_2O_3 microplates with an edge crack through the first five modes. With constant values of aspect ratio a/h, crack ratio c/a, and material index n, it is observed that the growth of material length scale ratio ℓ/h meaning h decreases as ℓ fixed is followed by the increase of the natural frequency in each mode. This observation can also be made from Table 1 where the numerical results for cases with size effects, i.e. $\ell/h \neq 0$ are presented. The reason for this phenomenon is that as the consideration of the size-dependent effect gets more pronounced, i.e. larger ℓ/h, the contribution of the non-classical terms to the structure's strain energy in Eq. (4) becomes proportionally significant. Therefore, the stiffness of the structure is considerably increased yielding higher vibrational frequencies as a result of the structural capacity improvement. It is worth commenting that the natural frequencies consistently increase as the modes change reflects the nature of the vibration problem regardless of size-dependent effects. For illustrative purposes, the first four mode shapes of simply-supported plates with an edge crack for specific geometry and material parameters of $a/h = 20, c/a = 0.5, \ell/h = 0.2, n = 5$ in which the size-dependent effects are considered are plotted in Fig. 6.

Similarly, as a parametric study, while Fig. 7 shows the effects of the material length scale ratio ℓ/h on the the natural frequencies of clamped-free Al/Al_2O_3 microplates with an edge crack, those effects on Al/Al_2O_3 microplates with a center crack are illustrated in Fig. 8. In the latter case, the plates are tested with different type of boundary conditions including simply-supported and clamped ones. As the clamped plates are enforced with

more constraints, the natural frequencies reach higher magnitudes due to the increase of the structure's stiffness.

Fig. 9 demonstrates the effects of the crack ratio c/a and the material length scale ratio ℓ/h on the natural frequencies of Al/Al_2O_3 microplates with center crack through modes $(a/h = 20, n = 1)$. As it can be expected, although the variations of natural frequencies against the crack ratio are of similar trends, the results generated from cases with $\ell/h \equiv 0$ are 25% - 30% smaller than those calculated from the approach in which the SGT is considered to account for size-dependent effects $(\ell/h = 0.2)$. Meanwhile, the increase of the crack ratio c/a which means a larger crack is prescribed in the plate is generally followed by the decline in vibrational frequencies as a result of the structure being weaken. In addition, one may notice that while the natural frequencies of the first and third modes vary slightly as crack length grows, those of the second and fourth modes drop significantly. This is due to the fact that the mode shapes in the latter case are of crack-opening configurations while the crack paths in the former cases remain closed. It is interesting to see that even though the boundary conditions are different, mode shapes corresponding to the SSSS plates are similar to those of CCCC ones shown in Fig. 12 in terms of crack opening.

A more comprehensive illustration of the effects of the material length scale ratio ℓ/h, aspect ratio a/h, and material index n on the fundamental frequency of the plate can be found in Fig. 10. As can be further observed here, with other geometrical parameter fixed, the increase of the material index n weakens the structural stiffness which causes the decrease in vibrational frequencies. This is a results of the volume fraction or, in order word, the proportion of ceramic phase (Al_2O_3) being reduced and replaced by the metal phase (Al) with lower elasticity modulus as n increased. One can also interpret this trend by looking at the material distribution of FG plates which is, in this study, governed by the rule of mixtures shown in Eq. (15). For the purpose of visual illustration, Fig. 11 shows the first four mode shapes of a clamped-free plate with an edge crack while those of a fully-clamped plate with a center crack are plotted in Fig. 12.

4.3. Circular and annular microplates with cracks

A number of numerical studies the vibration behaviours of circular and annular small-scale FG plates with cracks whose geometries depicted in Fig. 13 will be discussed in this part of the section. In order to present the results in an efficient manner, this normalisation is employed $\bar{\omega} = \omega \dfrac{R^2}{h}\sqrt{\dfrac{\rho_c}{E_c}}$. Fig. 14 presents the effects of the material length scale ratio ℓ/h on the natural frequencies of the simply-supported circular plate with a center crack. Similar to the previous part where the rectangular plates are considered, the increase in material length scale ratio leads to the rise of the vibrational frequencies. This is attributed to the inclusion of the strain gradient terms in the strain energy density of the small-scale plates which increases the magnitude of the structural stiffness. The first four mode shapes of the simply-supported microplates with a center crack and specific geometry and material parameters are plotted in Fig. 15.

For annular plates, only one half of the symmetric structure is analysed due to the fact that this consideration significantly reduces the complexity of geometry representations in

IGA and also the computational effort of solving procedure. Fig. 16 shows the effects of the material length scale ratio ℓ/h on the natural frequencies of the microplates in which the inner perimeter is free from constraints while the clamped boundary condition is apply at the outer circle of the annulus. In addition, Fig. 17 illustrates a more comprehensive observation of how geometry and material factors effect the vibrational behaviours in which the variation of the plate's fundamental frequencies against the changes of material length scale ratio ℓ/h, aspect ratio R/h, and material index n are given. Meanwhile, Fig. 18 describes the first four mode shapes the annular plate subjected to clamped-free boundary condition with a center crack and specific geometry and material parameters.

5. Concluding remarks

The strain gradient theory with one material length scale parameter and an additional micro-inertia term was employed together with the extended isogeometric analysis to investigate the vibration behaviours of functionally graded microplates with cracks. The displacement field was described using the refined plate theory with four unknowns which results in a sixth-order problem with C^2-continuity requirement. This condition was effectively fulfilled by the extended isogeometric analysis that possesses highly smooth basis functions of NURBS with new enrichment functions. Meanwhile, the size-dependent effects in small-scale plates which classical continuum theory failed to capture were efficiently predicted by the strain gradient theory. The benchmark results showed significant departure from those generated by the classical theory. The parametric studies showed that the inclusion of material length scale and the addition of micro-inertia term resulted in increases of vibration frequencies when the size of the plates become smaller. Besides, a completely different scenario was observed when the material index n of the functionally graded material increases and it decreases the vibration frequencies. In addition, the influence of the aspect ratio a/h was also investigated which shows a remarkable effect on the frequencies of thin plates but less pronounced for thick plates. Furthermore, the vibration mode shapes had strong impacts on the corresponding frequencies when crack length increases, especially for open-crack cases. Meanwhile, those were less significant for configurations with cracks remained closed.

Acknowledgement

The first and last authors gratefully acknowledge the financial support from the Northumbria University via the Researcher Development Framework. The second and the first authors would like to acknowledge the financial support from CONICYT REDI170090 and the Santander Universities Mobility Grant for the research visit at the University of Chile in March 2018.

References

[1] R. S. Lakes, Experimental microelasticity of two porous solids, International Journal of Solids and Structures 22 (1) (1986) 55–63. doi:10.1016/0020-7683(86)90103-4.

[2] H. C. Park, R. S. Lakes, Cosserat micromechanics of human bone: Strain redistribution by a hydration sensitive constituent, Journal of Biomechanics 19 (5) (1986) 385–397. doi:10.1016/0021-9290(86)90015-1.
[3] R. D. Mindlin, Micro-structure in linear elasticity, Archive for Rational Mechanics and Analysis 16 (1) (1964) 51–78. doi:10.1007/BF00248490.
[4] E. Cosserat, F. Cosserat, Theorie des Corps Deformables, Hermann et Fils, 1909.
[5] R. A. Toupin, Elastic materials with couple-stresses, Archive for Rational Mechanics and Analysis 11 (1) (1962) 385–414. doi:10.1007/BF00253945.
[6] W. T. Koiter, Couple-Stress in the Theory of Elasticity, Proc.K.Ned.Akad.Wet 67 (1964) 17–44.
[7] P. A. Gourgiotis, H. G. Georgiadis, I. Neocleous, On the reflection of waves in half-spaces of microstructured materials governed by dipolar gradient elasticity, Wave Motion 50 (3) (2013) 437–455. doi:10.1016/j.wavemoti.2012.10.004.
[8] A. T. Karttunen, J. N. Reddy, J. Romanoff, Closed-form solution for circular microstructure-dependent Mindlin plates, Acta Mechanica 228 (1) (2017) 323–331. doi:10.1007/s00707-016-1702-6.
[9] B. Reinaldo Goncalves, J. Romanoff, Size-dependent modelling of elastic sandwich beams with prismatic cores, International Journal of Solids and Structures 136-137 (2018) 28–37. doi:10.1016/j.ijsolstr.2017.12.001.
[10] L. C. Trinh, H. X. Nguyen, T. P. Vo, T.-K. Nguyen, Size-dependent behaviour of functionally graded microbeams using various shear deformation theories based on the modified couple stress theory, Composite Structures 154 (2016) 556–572. doi:10.1016/j.compstruct.2016.07.033.
[11] E. Atroshchenko, J. S. Hale, J. A. Videla, S. Potapenko, S. P. A. Bordas, Micro-structured materials: Inhomogeneities and imperfect interfaces in plane micropolar elasticity, a boundary element approach, Engineering Analysis with Boundary Elements 83 (2017) 195–203. doi:10.1016/j.enganabound.2017.07.023.
[12] E. Atroshchenko, S. P. A. Bordas, Fundamental solutions and dual boundary element methods for fracture in plane Cosserat elasticity, Proceedings. Mathematical, Physical, and Engineering Sciences 471 (2179) (2015) 20150216. doi:10.1098/rspa.2015.0216.
[13] A. T. Karttunen, J. N. Reddy, J. Romanoff, Micropolar modeling approach for periodic sandwich beams, Composite Structures 185 (2018) 656–664. doi:10.1016/j.compstruct.2017.11.064.
[14] H. Askes, E. C. Aifantis, Gradient elasticity in statics and dynamics: An overview of formulations, length scale identification procedures, finite element implementations and new results, International Journal of Solids and Structures 48 (13) (2011) 1962–1990. doi:10.1016/j.ijsolstr.2011.03.006.
[15] H. G. Georgiadis, I. Vardoulakis, E. G. Velgaki, Dispersive Rayleigh-Wave Propagation in Microstructured Solids Characterized by Dipolar Gradient Elasticity, Journal of Elasticity 74 (1) (2004) 17–45. doi:10.1023/B:ELAS.0000026094.95688.c5.
[16] H. G. Georgiadis, D. S. Anagnostou, Problems of the Flamant–Boussinesq and Kelvin Type in Dipolar Gradient Elasticity, Journal of Elasticity 90 (1) (2008) 71–98. doi:10.1007/s10659-007-9129-x.
[17] M. Lazar, G. A. Maugin, Nonsingular stress and strain fields of dislocations and disclinations in first strain gradient elasticity, International Journal of Engineering Science 43 (13) (2005) 1157–1184. doi:10.1016/j.ijengsci.2005.01.006.
[18] P. A. Gourgiotis, H. G. Georgiadis, Torsional and SH surface waves in an isotropic and homogenous elastic half-space characterized by the Toupin–Mindlin gradient theory, International Journal of Solids and Structures 62 (2015) 217–228. doi:10.1016/j.ijsolstr.2015.02.032.
[19] G. A. Maugin, A. Miled, Solitary waves in micropolar elastic crystals, International Journal of Engineering Science 24 (9) (1986) 1477–1499. doi:10.1016/0020-7225(86)90158-8.
[20] H. Gao, Y. Huang, W. D. Nix, J. W. Hutchinson, Mechanism-based strain gradient plasticity— I. Theory, Journal of the Mechanics and Physics of Solids 47 (6) (1999) 1239–1263. doi:10.1016/S0022-5096(98)00103-3.
[21] Y. Huang, H. Gao, W. D. Nix, J. W. Hutchinson, Mechanism-based strain gradient plasticity—II. Analysis, Journal of the Mechanics and Physics of Solids 48 (1) (2000) 99–128. doi:10.1016/S0022-5096(99)00022-8.

[22] P. A. Gourgiotis, H. G. Georgiadis, Plane-strain crack problems in microstructured solids governed by dipolar gradient elasticity, Journal of the Mechanics and Physics of Solids 57 (11) (2009) 1898–1920. doi:10.1016/j.jmps.2009.07.005.

[23] F. Putar, J. Sorić, T. Lesičar, Z. Tonković, Damage modeling employing strain gradient continuum theory, International Journal of Solids and Structures 120 (2017) 171–185. doi:10.1016/j.ijsolstr.2017.04.039.

[24] S. Papargyri-Beskou, D. E. Beskos, Static, stability and dynamic analysis of gradient elastic flexural Kirchhoff plates, Archive of Applied Mechanics 78 (8) (2008) 625–635. doi:10.1007/s00419-007-0166-5.

[25] J. N. Reddy, A Simple Higher-Order Theory for Laminated Composite Plates, Journal of Applied Mechanics 51 (4) (1984) 745–752. doi:10.1115/1.3167719.

[26] N. R. Senthilnathan, S. P. Lim, K. H. Lee, S. T. Chow, Buckling of Shear-Deformable Plates, AIAA Journal 25 (9) (1987) 1268–1271. doi:10.2514/3.48742.

[27] A. T. Karttunen, R. von Hertzen, J. N. Reddy, J. Romanoff, Bridging plate theories and elasticity solutions, International Journal of Solids and Structures 106-107 (2017) 251–263. doi:10.1016/j.ijsolstr.2016.09.037.

[28] J. N. Reddy, Theory and Analysis of Elastic Plates and Shells, 2nd Edition, CRC Press, 2006.

[29] T.-K. Nguyen, T. P. Vo, H.-T. Thai, Vibration and buckling analysis of functionally graded sandwich plates with improved transverse shear stiffness based on the first-order shear deformation theory, Proceedings of the Institution of Mechanical Engineers, Part C: Journal of Mechanical Engineering Science 228 (12) (2014) 2110–2131. doi:10.1177/0954406213516088.

[30] N. V. Nguyen, H. X. Nguyen, D.-H. Phan, H. Nguyen-Xuan, A polygonal finite element method for laminated composite plates, International Journal of Mechanical Sciences 133 (2017) 863–882. doi:10.1016/j.ijmecsci.2017.09.032.

[31] L. Zhang, B. Liang, S. Zhou, B. Wang, Y. Xue, An application of a size-dependent model on microplate with elastic medium based on strain gradient elasticity theory, Meccanica 52 (1-2) (2017) 251–262. doi:10.1007/s11012-016-0393-3.

[32] S. J. V. Frankland, A. Caglar, D. W. Brenner, M. Griebel, Molecular simulation of the influence of chemical cross–links on the shear strength of carbon nanotube–polymer interfaces, The Journal of Physical Chemistry B 106 (12) (2002) 3046–3048. doi:10.1021/jp015591.

[33] X. Ji, A. Li, S. Zhou, A comparison of strain gradient theories with applications to the functionally graded circular micro-plate, Applied Mathematical Modelling 49 (2017) 124–143. doi:10.1016/j.apm.2017.04.021.

[34] S. Khakalo, J. Niiranen, Form II of Mindlin's second strain gradient theory of elasticity with a simplification: For materials and structures from nano- to macro-scales, European Journal of Mechanics - A/Solids 71 (2018) 292–319. doi:10.1016/j.euromechsol.2018.02.013.

[35] S. Khakalo, J. Niiranen, Gradient-elastic stress analysis near cylindrical holes in a plane under bi-axial tension fields, International Journal of Solids and Structures 110–111 (2017) 351–366. doi:10.1016/j.ijsolstr.2016.10.025.

[36] T. Hughes, J. Cottrell, Y. Bazilevs, Isogeometric analysis: Cad, finite elements, nurbs, exact geometry and mesh refinement, Computer Methods in Applied Mechanics and Engineering 194 (39–41) (2005) 4135 – 4195. doi:http://dx.doi.org/10.1016/j.cma.2004.10.008.

[37] J. A. Cottrell, T. J. R. Hughes, Y. Bazilevs, Isogeometric Analysis: Toward Integration of CAD and FEA, 1st Edition, Wiley Publishing, 2009.

[38] A. V. Vuong, C. Heinrich, B. Simeon, ISOGAT: A 2d tutorial MATLAB code for Isogeometric Analysis, Computer Aided Geometric Design 27 (8) (2010) 644–655. doi:10.1016/j.cagd.2010.06.006.

[39] C. de Falco, A. Reali, R. Vázquez, GeoPDEs: A research tool for Isogeometric Analysis of PDEs, Advances in Engineering Software 42 (12) (2011) 1020–1034. doi:10.1016/j.advengsoft.2011.06.010.

[40] V. P. Nguyen, C. Anitescu, S. P. A. Bordas, T. Rabczuk, Isogeometric analysis: An overview and computer implementation aspects, Mathematics and Computers in Simulation 117 (2015) 89–116. doi:

10.1016/j.matcom.2015.05.008.
[41] H. X. Nguyen, T. N. Nguyen, M. Abdel-Wahab, S. P. A. Bordas, H. Nguyen-Xuan, T. P. Vo, A refined quasi-3d isogeometric analysis for functionally graded microplates based on the modified couple stress theory, Computer Methods in Applied Mechanics and Engineering 313 (2017) 904–940. doi:10.1016/j.cma.2016.10.002.
[42] H. X. Nguyen, E. Atroshchenko, H. Nguyen-Xuan, T. P. Vo, Geometrically nonlinear isogeometric analysis of functionally graded microplates with the modified couple stress theory, Computers & Structures 193 (2017) 110–127. doi:10.1016/j.compstruc.2017.07.017.
[43] V. Balobanov, J. Niiranen, Locking-free variational formulations and isogeometric analysis for the Timoshenko beam models of strain gradient and classical elasticity, Computer Methods in Applied Mechanics and Engineering 339 (2018) 137–159. doi:10.1016/j.cma.2018.04.028.
[44] S. Thai, H.-T. Thai, T. P. Vo, V. I. Patel, Size-dependant behaviour of functionally graded microplates based on the modified strain gradient elasticity theory and isogeometric analysis, Computers & Structures 190 (2017) 219–241. doi:10.1016/j.compstruc.2017.05.014.
[45] S. Thai, H.-T. Thai, T. P. Vo, H. Nguyen-Xuan, Nonlinear static and transient isogeometric analysis of functionally graded microplates based on the modified strain gradient theory, Engineering Structures 153 (2017) 598–612. doi:10.1016/j.engstruct.2017.10.002.
[46] N.-T. Nguyen, D. Hui, J. Lee, H. Nguyen-Xuan, An efficient computational approach for size-dependent analysis of functionally graded nanoplates, Computer Methods in Applied Mechanics and Engineering 297 (2015) 191 – 218. doi:http://dx.doi.org/10.1016/j.cma.2015.07.021.
[47] N. Moes, J. Dolbow, T. Belytschko, A finite element method for crack growth without remeshing, International Journal for Numerical Methods in Engineering 46 (1) (1999) 131–150. doi:10.1002/(SICI)1097-0207(19990910)46:1<131::AID-NME726>3.0.CO;2-J.
[48] D. J. Benson, Y. Bazilevs, E. De Luycker, M.-C. Hsu, M. Scott, T. J. R. Hughes, T. Belytschko, A generalized finite element formulation for arbitrary basis functions: From isogeometric analysis to XFEM, International Journal for Numerical Methods in Engineering 83 (6) (2010) 765–785. doi:10.1002/nme.2864.
[49] E. De Luycker, D. J. Benson, T. Belytschko, Y. Bazilevs, M. C. Hsu, X-FEM in isogeometric analysis for linear fracture mechanics, International Journal for Numerical Methods in Engineering 87 (6) (2011) 541–565. doi:10.1002/nme.3121.
[50] S. S. Ghorashi, N. Valizadeh, S. Mohammadi, Extended isogeometric analysis for simulation of stationary and propagating cracks, International Journal for Numerical Methods in Engineering 89 (9) (2012) 1069–1101. doi:10.1002/nme.3277.
[51] B. Stahl, L. M. Keer, Vibration and stability of cracked rectangular plates, International Journal of Solids and Structures 8 (1) (1972) 69–91. doi:10.1016/0020-7683(72)90052-2.
[52] M. Bachene, R. Tiberkak, S. Rechak, Vibration analysis of cracked plates using the extended finite element method, Archive of Applied Mechanics 79 (3) (2009) 249–262. doi:10.1007/s00419-008-0224-7.
[53] S. Natarajan, P. M. Baiz, S. Bordas, T. Rabczuk, P. Kerfriden, Natural frequencies of cracked functionally graded material plates by the extended finite element method, Composite Structures 93 (11) (2011) 3082–3092. doi:10.1016/j.compstruct.2011.04.007.
[54] L. V. Tran, H. A. Ly, J. Lee, M. A. Wahab, H. Nguyen-Xuan, Vibration analysis of cracked FGM plates using higher-order shear deformation theory and extended isogeometric approach, International Journal of Mechanical Sciences 96–97 (2015) 65–78. doi:10.1016/j.ijmecsci.2015.03.003.
[55] S. Liu, T. Yu, L. V. Lich, S. Yin, T. Q. Bui, Size effect on cracked functional composite micro-plates by an XIGA-based effective approach, Meccanica (2018) 1–22doi:10.1007/s11012-018-0848-9.
[56] T. Nakamura, T. Wang, S. Sampath, Determination of properties of graded materials by inverse analysis and instrumented indentation, Acta Materialia 48 (17) (2000) 4293–4306. doi:10.1016/S1359-6454(00)00217-2.
[57] T. Mori, K. Tanaka, Average stress in matrix and average elastic energy of materials with misfitting inclusions, Acta Metallurgica 21 (5) (1973) 571–574. doi:10.1016/0001-6160(73)90064-3.
[58] L. Piegl, W. Tiller, The NURBS Book, Monographs in Visual Communication, Springer Berlin Heidel-

berg, Berlin, Heidelberg, 1997.

[59] S. Bordas, P. V. Nguyen, C. Dunant, A. Guidoum, H. Nguyen-Dang, An extended finite element library, International Journal for Numerical Methods in Engineering 71 (6) (2007) 703–732. doi:10.1002/nme.1966.

[60] G. Sciarra, S. Vidoli, Asymptotic Fracture Modes in Strain-Gradient Elasticity: Size Effects and Characteristic Lengths for Isotropic Materials, Journal of Elasticity 113 (1) (2013) 27–53. doi:10.1007/s10659-012-9409-y.

[61] C. S. Huang, O. G. McGee, M. J. Chang, Vibrations of cracked rectangular FGM thick plates, Composite Structures 93 (7) (2011) 1747–1764. doi:10.1016/j.compstruct.2011.01.005.

Appendix A Strain gradient components

$$\boldsymbol{\kappa}_x = \left\{ \begin{array}{c} \kappa_{xxx} \\ \kappa_{xyy} \\ 2\kappa_{xyz} \\ 2\kappa_{xxz} \\ 2\kappa_{xxy} \end{array} \right\}, \boldsymbol{\kappa}_x^0 = \left\{ \begin{array}{c} u_{0,xx} \\ v_{0,xy} \\ w_{s,xy} \\ w_{s,xx} \\ u_{0,xy} + v_{0,xx} \end{array} \right\}, \boldsymbol{\kappa}_x^1 = \left\{ \begin{array}{c} -w_{b,xxx} \\ -w_{b,xyy} \\ 0 \\ 0 \\ -2w_{b,xxy} \end{array} \right\}, \boldsymbol{\kappa}_x^2 = \left\{ \begin{array}{c} w_{s,xxx} \\ w_{s,xyy} \\ 0 \\ 0 \\ 2w_{s,xxy} \end{array} \right\}, \boldsymbol{\kappa}_x^3 = \left\{ \begin{array}{c} 0 \\ 0 \\ w_{s,xy} \\ w_{s,xx} \\ 0 \end{array} \right\}, \boldsymbol{\kappa}_x^4 = \left\{ \begin{array}{c} 0 \\ 0 \\ 0 \\ 0 \\ 0 \end{array} \right\} \tag{34}$$

$$\boldsymbol{\kappa}_y = \left\{ \begin{array}{c} \kappa_{yxx} \\ \kappa_{yyy} \\ 2\kappa_{yyz} \\ 2\kappa_{yxz} \\ 2\kappa_{yxy} \end{array} \right\}, \boldsymbol{\kappa}_y^0 = \left\{ \begin{array}{c} u_{0,xy} \\ v_{0,yy} \\ w_{s,yy} \\ w_{s,xy} \\ u_{0,yy} + v_{0,xy} \end{array} \right\}, \boldsymbol{\kappa}_y^1 = \left\{ \begin{array}{c} -w_{b,xyy} \\ -w_{b,yyy} \\ 0 \\ 0 \\ -2w_{b,xyy} \end{array} \right\}, \boldsymbol{\kappa}_y^2 = \left\{ \begin{array}{c} w_{s,xyy} \\ w_{s,yyy} \\ 0 \\ 0 \\ 2w_{s,xyy} \end{array} \right\}, \boldsymbol{\kappa}_y^3 = \left\{ \begin{array}{c} 0 \\ 0 \\ w_{s,yy} \\ w_{s,xy} \\ 0 \end{array} \right\}, \boldsymbol{\kappa}_y^4 = \left\{ \begin{array}{c} 0 \\ 0 \\ 0 \\ 0 \\ 0 \end{array} \right\} \tag{35}$$

$$\boldsymbol{\kappa}_z = \left\{ \begin{array}{c} \kappa_{zxx} \\ \kappa_{zyy} \\ 2\kappa_{zyz} \\ 2\kappa_{zxz} \\ 2\kappa_{zxy} \end{array} \right\}, \boldsymbol{\kappa}_z^0 = \left\{ \begin{array}{c} -w_{b,xx} \\ -w_{b,yy} \\ 0 \\ 0 \\ -2w_{b,xy} \end{array} \right\}, \boldsymbol{\kappa}_z^1 = \left\{ \begin{array}{c} 0 \\ 0 \\ 0 \\ 0 \\ 0 \end{array} \right\}, \boldsymbol{\kappa}_z^2 = \left\{ \begin{array}{c} 0 \\ 0 \\ 0 \\ 0 \\ 0 \end{array} \right\}, \boldsymbol{\kappa}_z^3 = \left\{ \begin{array}{c} w_{s,xx} \\ w_{s,yy} \\ 0 \\ 0 \\ 2w_{s,xy} \end{array} \right\}, \boldsymbol{\kappa}_z^4 = \left\{ \begin{array}{c} 0 \\ 0 \\ w_{s,y} \\ w_{s,x} \\ 0 \end{array} \right\} \tag{36}$$

$$\kappa_{izz} = 0 \tag{37}$$

Appendix B B matrices

$$\mathbf{B}_A^m = \begin{bmatrix} \bar{R}_{A,x} & 0 & 0 & 0 \\ 0 & \bar{R}_{A,y} & 0 & 0 \\ \bar{R}_{A,y} & \bar{R}_{A,x} & 0 & 0 \end{bmatrix}, \quad \mathbf{B}_A^{b1} = \begin{bmatrix} 0 & 0 & -\bar{R}_{A,xx} & 0 \\ 0 & 0 & -\bar{R}_{A,yy} & 0 \\ 0 & 0 & -2\bar{R}_{A,xy} & 0 \end{bmatrix}, \quad \mathbf{B}_A^{b2} = \begin{bmatrix} 0 & 0 & 0 & \bar{R}_{A,xx} \\ 0 & 0 & 0 & \bar{R}_{A,yy} \\ 0 & 0 & 0 & 2\bar{R}_{A,xy} \end{bmatrix}, \tag{38a}$$

$$\mathbf{B}_A^s = \begin{bmatrix} 0 & 0 & 0 & \bar{R}_{A,x} \\ 0 & 0 & 0 & \bar{R}_{A,y} \end{bmatrix}, \tag{38b}$$

$$\mathbf{B}_A^{x0} = \begin{bmatrix} \bar{R}_{A,xx} & 0 & 0 & 0 \\ 0 & \bar{R}_{A,xy} & 0 & 0 \\ 0 & 0 & 0 & 0 \\ 0 & 0 & 0 & \bar{R}_{A,xy} \\ 0 & 0 & 0 & \bar{R}_{A,xx} \\ \bar{R}_{A,xy} & \bar{R}_{A,xx} & 0 & 0 \end{bmatrix}, \quad \mathbf{B}_A^{x1} = \begin{bmatrix} 0 & 0 & -\bar{R}_{A,xxx} & 0 \\ 0 & 0 & -\bar{R}_{A,xyy} & 0 \\ 0 & 0 & 0 & 0 \\ 0 & 0 & 0 & 0 \\ 0 & 0 & 0 & 0 \\ 0 & 0 & -2\bar{R}_{A,xxy} & 0 \end{bmatrix}, \tag{39a}$$

$$\mathbf{B}_A^{x2} = \begin{bmatrix} 0 & 0 & 0 & \bar{R}_{A,xxx} \\ 0 & 0 & 0 & \bar{R}_{A,xyy} \\ 0 & 0 & 0 & 0 \\ 0 & 0 & 0 & 0 \\ 0 & 0 & 0 & 0 \\ 0 & 0 & 0 & 2\bar{R}_{A,xxy} \end{bmatrix}, \quad \mathbf{B}_A^{x3} = \begin{bmatrix} 0 & 0 & 0 & 0 \\ 0 & 0 & 0 & 0 \\ 0 & 0 & 0 & 0 \\ 0 & 0 & 0 & \bar{R}_{A,xy} \\ 0 & 0 & 0 & \bar{R}_{A,xy} \\ 0 & 0 & 0 & 0 \end{bmatrix}, \quad \mathbf{B}_A^{x4} = [\mathbf{0}], \tag{39b}$$

$$\mathbf{B}_A^{y0} = \begin{bmatrix} \bar{R}_{A,xy} & 0 & 0 & 0 \\ 0 & \bar{R}_{A,yy} & 0 & 0 \\ 0 & 0 & 0 & 0 \\ 0 & 0 & 0 & \bar{R}_{A,yy} \\ 0 & 0 & 0 & \bar{R}_{A,xy} \\ \bar{R}_{A,yy} & \bar{R}_{A,xy} & 0 & 0 \end{bmatrix}, \quad \mathbf{B}_A^{y1} = \begin{bmatrix} 0 & 0 & -\bar{R}_{A,xyy} & 0 \\ 0 & 0 & -\bar{R}_{A,yyy} & 0 \\ 0 & 0 & 0 & 0 \\ 0 & 0 & 0 & 0 \\ 0 & 0 & 0 & 0 \\ 0 & 0 & -2\bar{R}_{A,xyy} & 0 \end{bmatrix}, \tag{39c}$$

$$\mathbf{B}_A^{y2} = \begin{bmatrix} 0 & 0 & 0 & \bar{R}_{A,xyy} \\ 0 & 0 & 0 & \bar{R}_{A,yyy} \\ 0 & 0 & 0 & 0 \\ 0 & 0 & 0 & 0 \\ 0 & 0 & 0 & 0 \\ 0 & 0 & 0 & 2\bar{R}_{A,xyy} \end{bmatrix}, \quad \mathbf{B}_A^{y3} = \begin{bmatrix} 0 & 0 & 0 & 0 \\ 0 & 0 & 0 & 0 \\ 0 & 0 & 0 & 0 \\ 0 & 0 & 0 & \bar{R}_{A,yy} \\ 0 & 0 & 0 & \bar{R}_{A,xy} \\ 0 & 0 & 0 & 0 \end{bmatrix}, \quad \mathbf{B}_A^{y4} = [\mathbf{0}], \tag{39d}$$

$$\mathbf{B}_A^{z0} = \begin{bmatrix} 0 & 0 & -\bar{R}_{A,xx} & 0 \\ 0 & 0 & -\bar{R}_{A,yy} & 0 \\ 0 & 0 & 0 & 0 \\ 0 & 0 & 0 & 0 \\ 0 & 0 & 0 & 0 \\ 0 & 0 & -2\bar{R}_{A,xy} & 0 \end{bmatrix}, \quad \mathbf{B}_A^{z1} = [\mathbf{0}], \quad \mathbf{B}_A^{z2} = [\mathbf{0}], \tag{39e}$$

$$\mathbf{B}_A^{z3} = \begin{bmatrix} 0 & 0 & 0 & \bar{R}_{A,xx} \\ 0 & 0 & 0 & \bar{R}_{A,yy} \\ 0 & 0 & 0 & 0 \\ 0 & 0 & 0 & 0 \\ 0 & 0 & 0 & 0 \\ 0 & 0 & 0 & 2\bar{R}_{A,xy} \end{bmatrix}, \quad \mathbf{B}_A^{z4} = \begin{bmatrix} 0 & 0 & 0 & 0 \\ 0 & 0 & 0 & 0 \\ 0 & 0 & 0 & 0 \\ 0 & 0 & 0 & \bar{R}_{A,y} \\ 0 & 0 & 0 & \bar{R}_{A,x} \\ 0 & 0 & 0 & 0 \end{bmatrix}, \tag{39f}$$

where $\bar{R}$ can be either standard basis functions or enrichment functions.

Appendix C Element stiffness matrices

$$\mathbf{K}_c^e = \int_{\Omega_e} \begin{Bmatrix} \mathbf{B}^m \\ \mathbf{B}^{b1} \\ \mathbf{B}^{b2} \end{Bmatrix}^T \begin{bmatrix} \mathbf{A} & \mathbf{B} & \mathbf{E} \\ \mathbf{B} & \mathbf{D} & \mathbf{F} \\ \mathbf{E} & \mathbf{F} & \mathbf{H} \end{bmatrix} \begin{Bmatrix} \mathbf{B}^m \\ \mathbf{B}^{b1} \\ \mathbf{B}^{b2} \end{Bmatrix} d\Omega_e, \tag{40}$$

$$\mathbf{K}_{gx}^e = \int_{\Omega_e} \begin{Bmatrix} \mathbf{B}^{x0} \\ \mathbf{B}^{x1} \\ \mathbf{B}^{x2} \\ \mathbf{B}^{x3} \\ \mathbf{B}^{x4} \end{Bmatrix}^T \begin{bmatrix} \mathbf{A}^g & \mathbf{B}^g & \mathbf{E}^g & \mathbf{G}^g & \mathbf{M}^g \\ \mathbf{B}^g & \mathbf{D}^g & \mathbf{F}^g & \mathbf{I}^g & \mathbf{N}^g \\ \mathbf{E}^g & \mathbf{F}^g & \mathbf{H}^g & \mathbf{J}^g & \mathbf{P}^g \\ \mathbf{G}^g & \mathbf{I}^g & \mathbf{J}^g & \mathbf{L}^g & \mathbf{Q}^g \\ \mathbf{M}^g & \mathbf{N}^g & \mathbf{P}^g & \mathbf{Q}^g & \mathbf{R}^g \end{bmatrix} \begin{Bmatrix} \mathbf{B}^{x0} \\ \mathbf{B}^{x1} \\ \mathbf{B}^{x2} \\ \mathbf{B}^{x3} \\ \mathbf{B}^{x4} \end{Bmatrix} d\Omega_e, \tag{41a}$$

$$\mathbf{K}_{gy}^e = \int_{\Omega_e} \begin{Bmatrix} \mathbf{B}^{y0} \\ \mathbf{B}^{y1} \\ \mathbf{B}^{y2} \\ \mathbf{B}^{y3} \\ \mathbf{B}^{y4} \end{Bmatrix}^T \begin{bmatrix} \mathbf{A}^g & \mathbf{B}^g & \mathbf{E}^g & \mathbf{G}^g & \mathbf{M}^g \\ \mathbf{B}^g & \mathbf{D}^g & \mathbf{F}^g & \mathbf{I}^g & \mathbf{N}^g \\ \mathbf{E}^g & \mathbf{F}^g & \mathbf{H}^g & \mathbf{J}^g & \mathbf{P}^g \\ \mathbf{G}^g & \mathbf{I}^g & \mathbf{J}^g & \mathbf{L}^g & \mathbf{Q}^g \\ \mathbf{M}^g & \mathbf{N}^g & \mathbf{P}^g & \mathbf{Q}^g & \mathbf{R}^g \end{bmatrix} \begin{Bmatrix} \mathbf{B}^{y0} \\ \mathbf{B}^{y1} \\ \mathbf{B}^{y2} \\ \mathbf{B}^{y3} \\ \mathbf{B}^{y4} \end{Bmatrix} d\Omega_e, \tag{41b}$$

$$\mathbf{K}_{gz}^e = \int_{\Omega_e} \begin{Bmatrix} \mathbf{B}^{z0} \\ \mathbf{B}^{z1} \\ \mathbf{B}^{z2} \\ \mathbf{B}^{z3} \\ \mathbf{B}^{z4} \end{Bmatrix}^T \begin{bmatrix} \mathbf{A}^g & \mathbf{B}^g & \mathbf{E}^g & \mathbf{G}^g & \mathbf{M}^g \\ \mathbf{B}^g & \mathbf{D}^g & \mathbf{F}^g & \mathbf{I}^g & \mathbf{N}^g \\ \mathbf{E}^g & \mathbf{F}^g & \mathbf{H}^g & \mathbf{J}^g & \mathbf{P}^g \\ \mathbf{G}^g & \mathbf{I}^g & \mathbf{J}^g & \mathbf{L}^g & \mathbf{Q}^g \\ \mathbf{M}^g & \mathbf{N}^g & \mathbf{P}^g & \mathbf{Q}^g & \mathbf{R}^g \end{bmatrix} \begin{Bmatrix} \mathbf{B}^{z0} \\ \mathbf{B}^{z1} \\ \mathbf{B}^{z2} \\ \mathbf{B}^{z3} \\ \mathbf{B}^{z4} \end{Bmatrix} d\Omega_e. \tag{41c}$$

Appendix D Element mass matrices

$$\mathbf{M}_c^e = \int_{\Omega_e} \tilde{\mathbf{R}}^T \tilde{\mathbf{m}} \tilde{\mathbf{R}} d\Omega_e \tag{42}$$

$$\mathbf{M}_{gx}^e = \frac{1}{3} d^2 \int_{\Omega_e} \tilde{\mathbf{R}}_{,x}^T \tilde{\mathbf{m}} \tilde{\mathbf{R}}_{,x}^T d\Omega_e, \tag{43a}$$

$$\mathbf{M}_{gy}^e = \frac{1}{3} d^2 \int_{\Omega_e} \tilde{\mathbf{R}}_{,y}^T \tilde{\mathbf{m}} \tilde{\mathbf{R}}_{,y}^T d\Omega_e, \tag{43b}$$

$$\mathbf{M}_{gz}^e = \frac{1}{3} d^2 \int_{\Omega_e} \tilde{\mathbf{R}}_{,z}^T \tilde{\mathbf{m}} \tilde{\mathbf{R}}_{,z}^T d\Omega_e, \tag{43c}$$

where

$$\tilde{\mathbf{R}} = \begin{bmatrix} \mathbf{R}_1 \\ \mathbf{R}_2 \\ \mathbf{R}_3 \end{bmatrix}, \tag{44a}$$

$$\mathbf{R}_1 = \begin{bmatrix} \bar{R}_A & 0 & 0 & 0 \\ 0 & 0 & -\bar{R}_{A,x} & 0 \\ 0 & 0 & 0 & \bar{R}_{A,x} \end{bmatrix}, \quad \mathbf{R}_2 = \begin{bmatrix} 0 & \bar{R}_A & 0 & 0 \\ 0 & 0 & -\bar{R}_{A,y} & 0 \\ 0 & 0 & 0 & \bar{R}_{A,y} \end{bmatrix}, \quad \mathbf{R}_3 = \begin{bmatrix} 0 & 0 & \bar{R}_A & 0 \\ 0 & 0 & 0 & \bar{R}_A \\ 0 & 0 & 0 & 0 \end{bmatrix}. \tag{44b}$$

Table 1: Normalised natural frequencies of SSSS Al/Al_2O_3 square plates with an edge crack

n	Method	ℓ/h	Mode				
			1	2	3	4	5
0	Ritz [61]	0	5.3790	11.4500	13.3200	16.1800	17.3200
	XFEM [53]	0	5.3870	11.4190	13.3590	—	
	XIGA-TSDT [54]	0	5.3643	11.4734	13.2801	16.2062	17.2927
	Present	0	5.4013	11.6012	13.2822	15.3834	17.3216
		0.2	6.6548	14.8945	15.9156	16.3371	19.3573
		0.4	9.3819	16.5765	19.5058	21.2259	22.3737
		0.6	12.6181	17.0482	19.6141	23.8053	28.5286
		0.8	15.9933	17.4653	19.7264	24.9174	32.6846
		1	17.8595	19.3634	19.8416	25.8765	33.9185
1	3D elasticity [61]	0	4.1150	8.8360	10.2400	13.3300	13.5200
	Ritz [61]	0	4.1220	8.8560	10.2500	13.3100	13.4900
	XFEM [53]	0	4.1220	8.5260	10.2850		
	XIGA-TSDT [54]	0	4.1119	8.8791	10.2131	13.3103	13.4946
	Present	0	4.1345	8.9400	10.2092	12.7727	13.3407
		0.2	5.2431	11.7900	12.9007	13.2175	16.0945
		0.4	7.5919	13.7657	16.2206	17.1983	18.5554
		0.6	10.3308	14.1609	16.3108	19.7674	23.3282
		0.8	13.1642	14.5086	16.4042	20.6946	27.1119
		1	14.8369	15.9821	16.5000	21.4940	28.1524
5	Ritz [61]	0	3.5110	7.3790	8.6210	10.4900	11.1700
	XFEM [53]	0	3.6260	7.4150	8.5660		
	XIGA-TSDT [54]	0	3.5018	7.3980	8.5912	10.4928	11.1511
	Present	0	3.5289	7.5199	8.5991	9.9608	11.1737
		0.2	4.3602	9.7714	10.3137	10.6874	12.5581
		0.4	6.1475	10.7351	12.6574	14.0349	14.4805
		0.6	8.2635	11.0441	12.7279	15.4147	18.8640
		0.8	10.4694	11.3157	12.8007	16.1391	21.1315
		1	11.5719	12.6717	12.8755	16.7637	21.9454
10	Ritz [61]	0	3.3880	7.0620	8.2890	9.5690	10.7100
	XFEM [53]	0	3.4090	7.0590	8.2210		
	XIGA-TSDT [54]	0	3.3773	7.0792	8.2582	9.5750	10.6887
	Present	0	3.4068	7.2173	8.2690	9.0874	10.7259
		0.2	4.1387	9.2388	9.4179	10.1306	11.4478
		0.4	5.7298	9.7933	11.5371	13.0854	13.2137
		0.6	7.6340	10.0738	11.6013	14.0628	17.4656
		0.8	9.6308	10.3210	11.6677	14.7221	19.2907
		1	10.5543	11.6304	11.7359	15.2906	20.0274

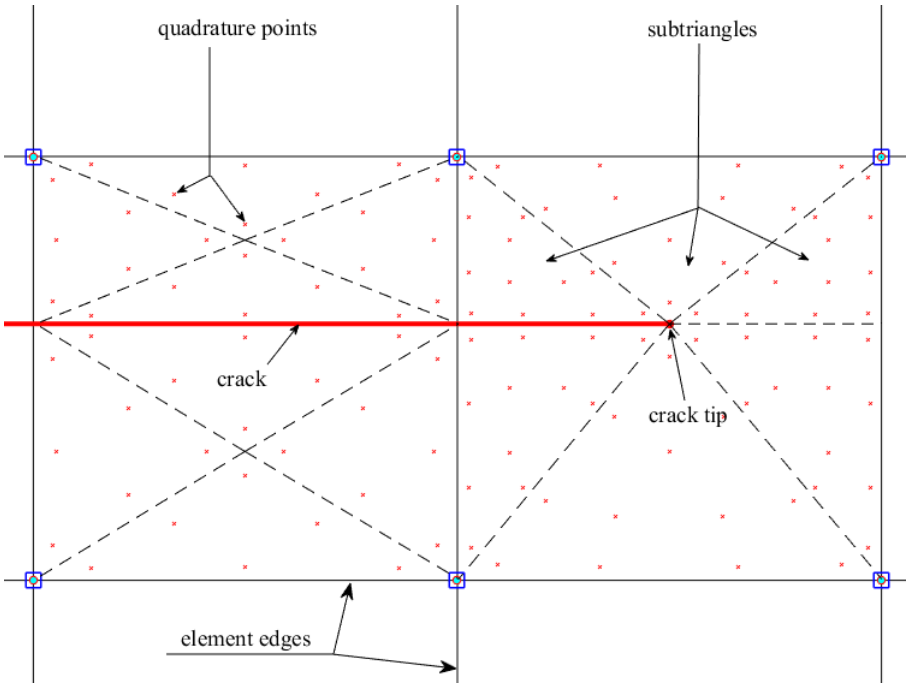

Figure 1: Sub-triangles for element cut by crack path and tip element.

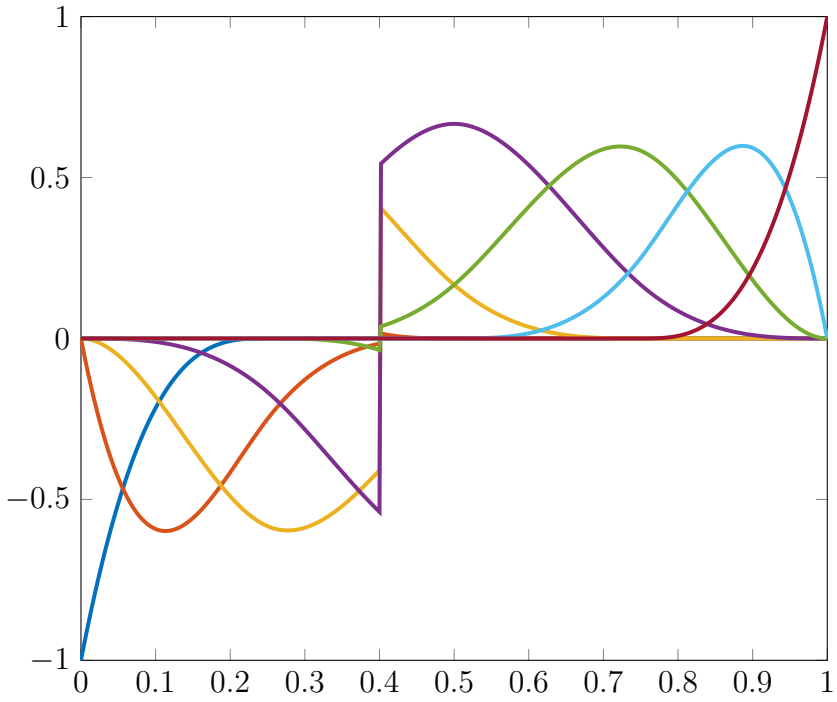

(a) The basis functions

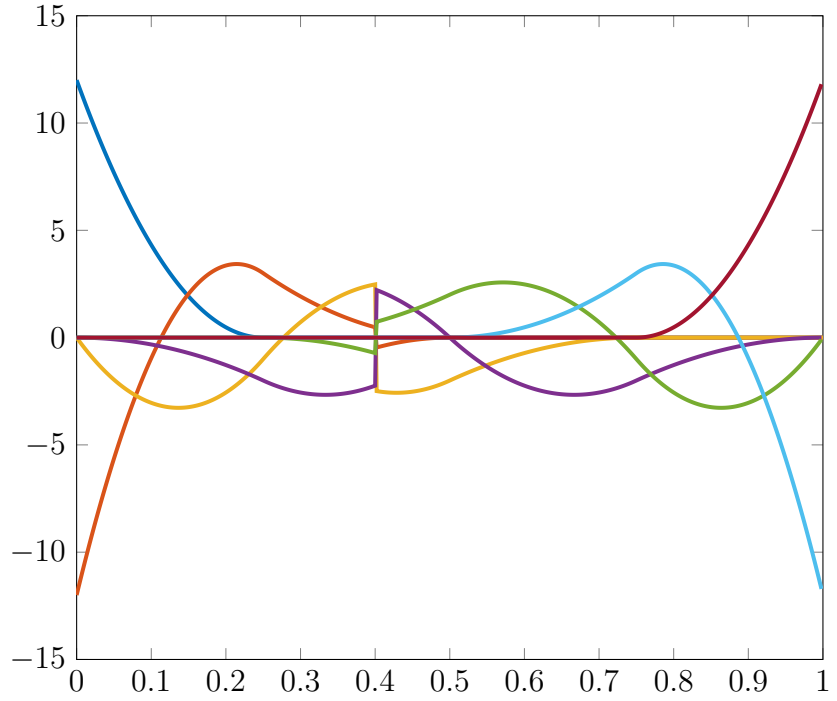

(b) The first derivatives of basis functions

Figure 2: Product of the Heaviside function H at $\xi = 0.4$ with the B-spline basis functions and its derivatives with the knot vector $\boldsymbol{\Xi} = \left\{0, 0, 0, 0, \frac{1}{4}, \frac{1}{2}, \frac{3}{4}, 1, 1, 1, 1\right\}$.

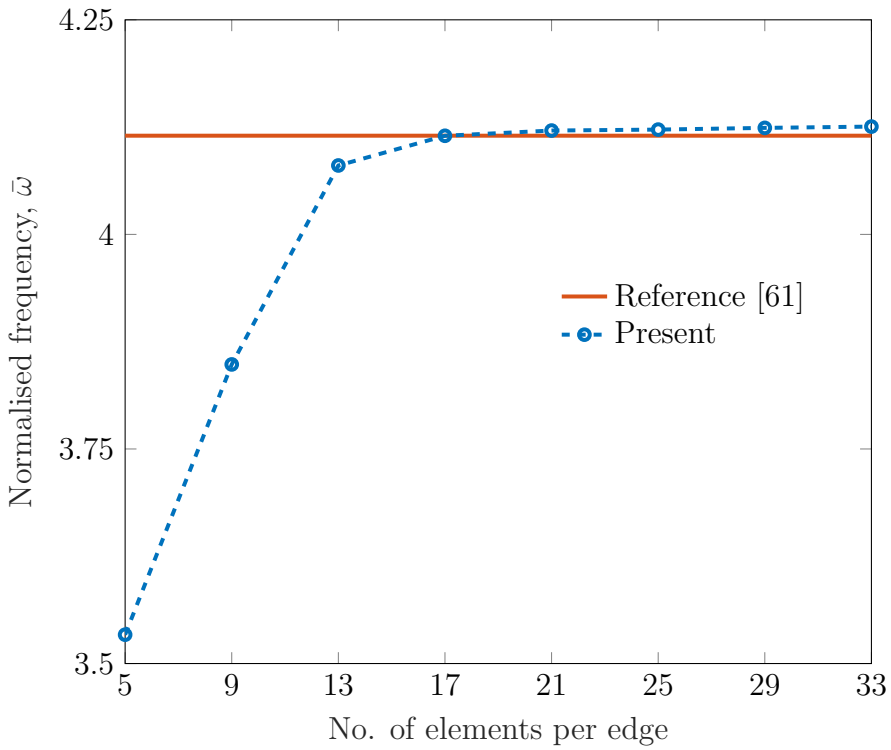

Figure 3: Convergence of fundamental frequency of simply-supported Al/Al_2O_3 square plates with different meshes, $a/h = 10, c/a = 0.5, n = 0$.

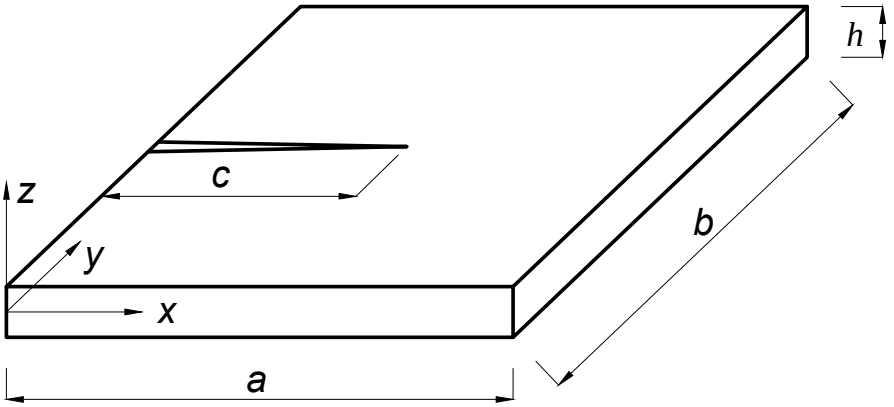

(a) Edge crack

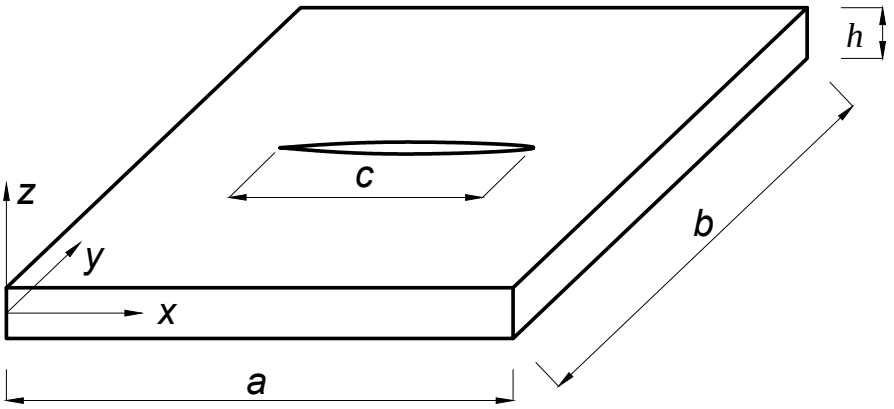

(b) Center crack

Figure 4: Geometry of square plates with cracks.

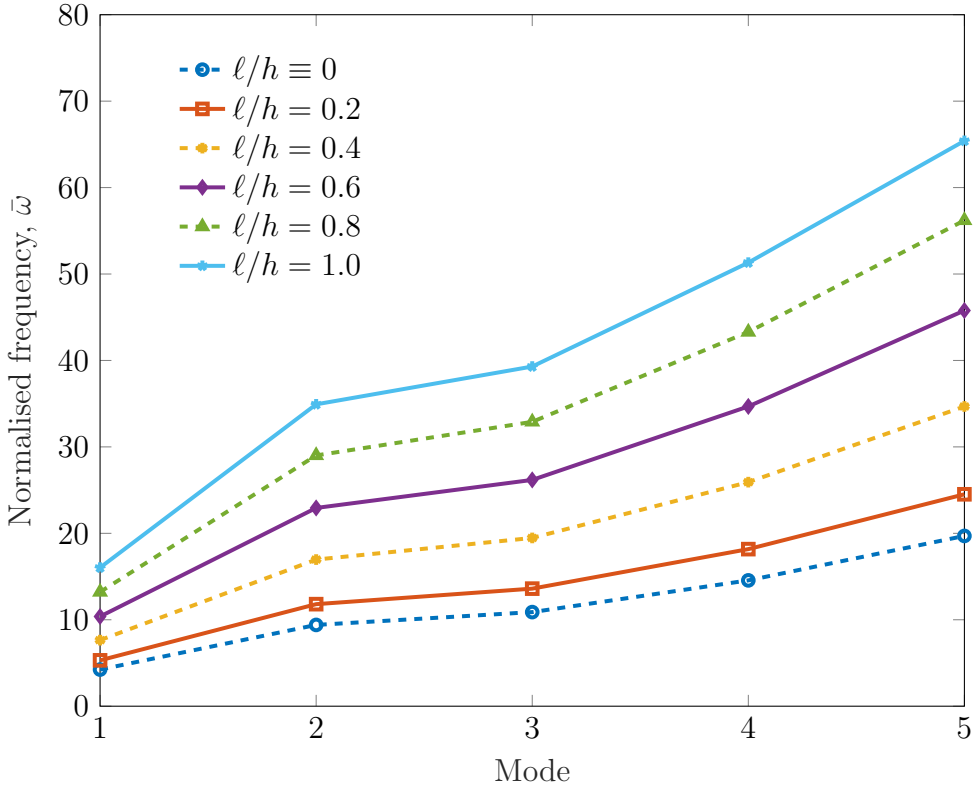

Figure 5: Effects of material length scale ratio ℓ/h on the natural frequencies of SSSS Al/Al_2O_3 square plates with an edge crack ($a/h = 100$, $c/a = 0.5$, $n = 1$).

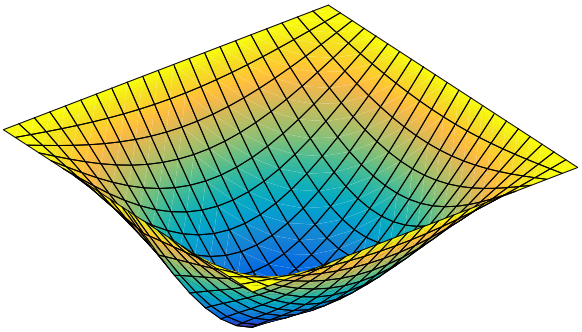

(a) Mode 1

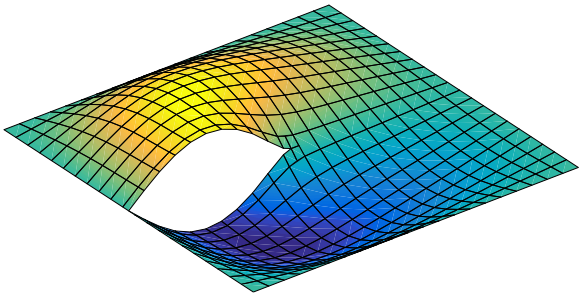

(b) Mode 2

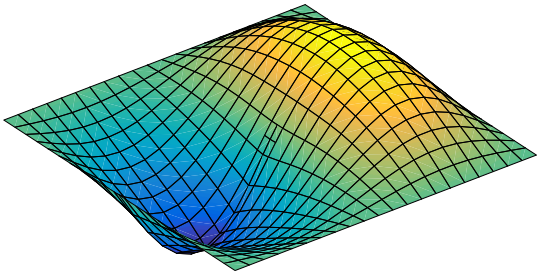

(c) Mode 3

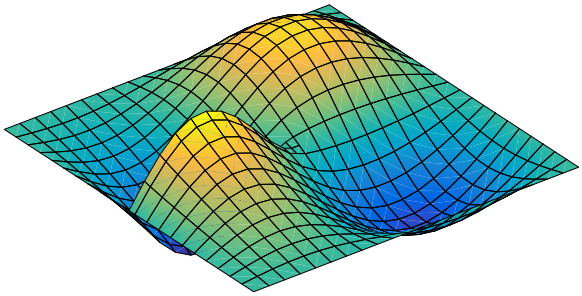

(d) Mode 4

Figure 6: The first four mode shapes of SSSS Al/Al_2O_3 with an edge crack.

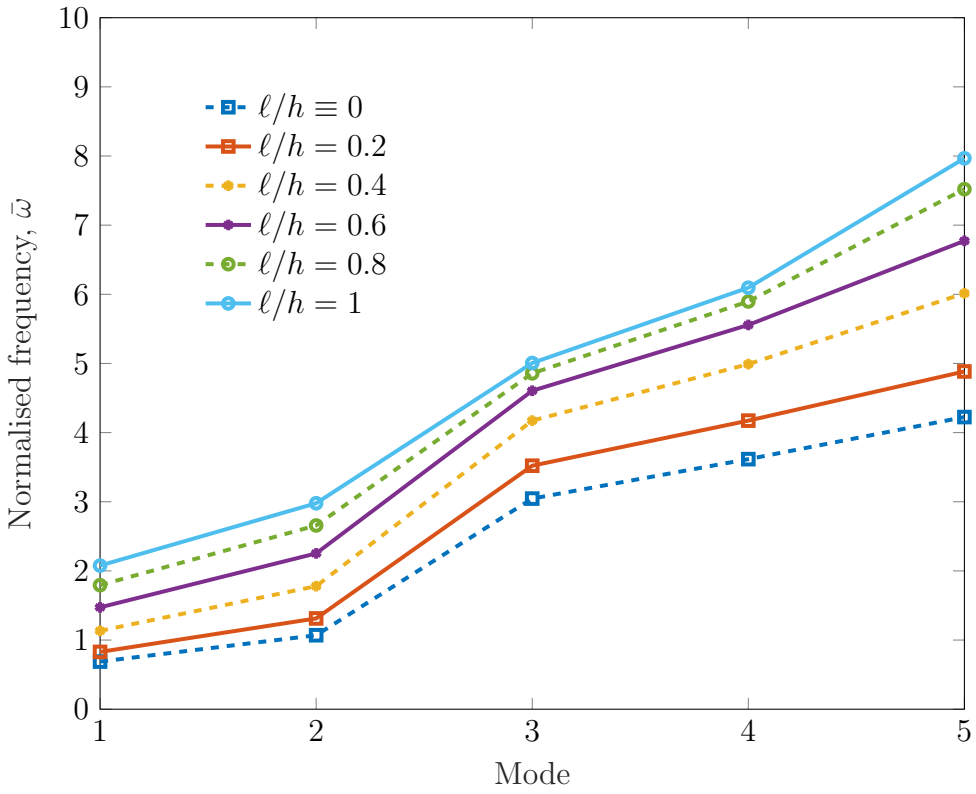

Figure 7: Effects of material length scale ratio ℓ/h on the natural frequencies of CFFF Al/Al_2O_3 square plates with an edge crack ($a/h = 20$, $c/a = 0.5$, $n = 5$).

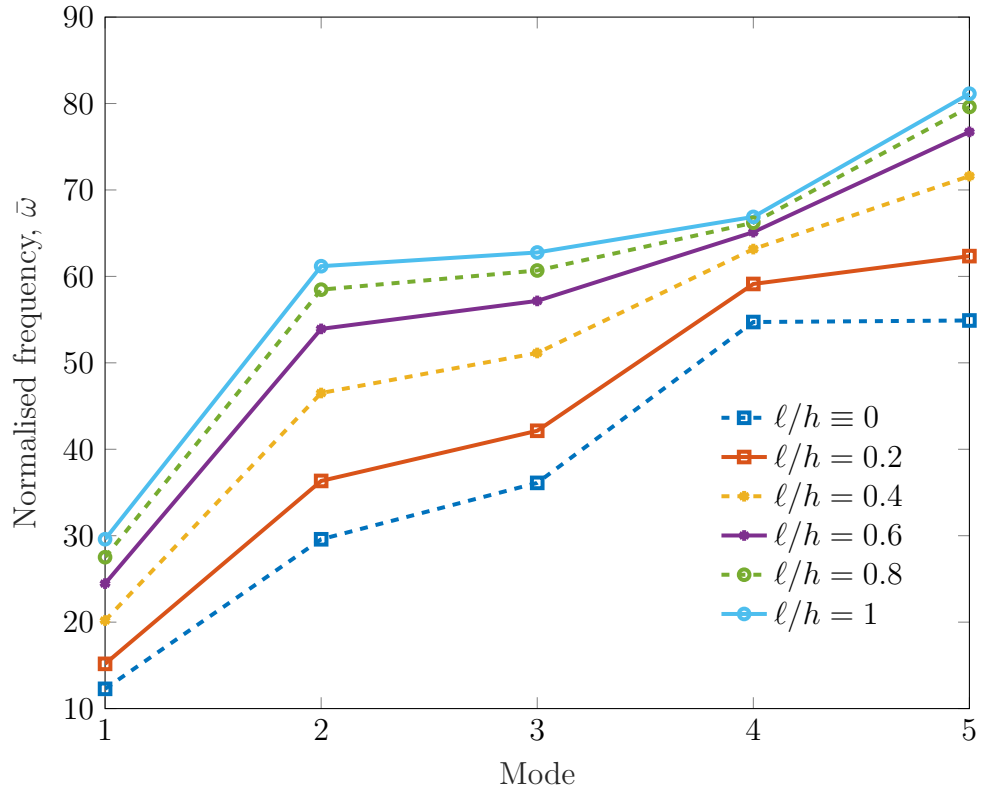

(a) Simply-supported plate

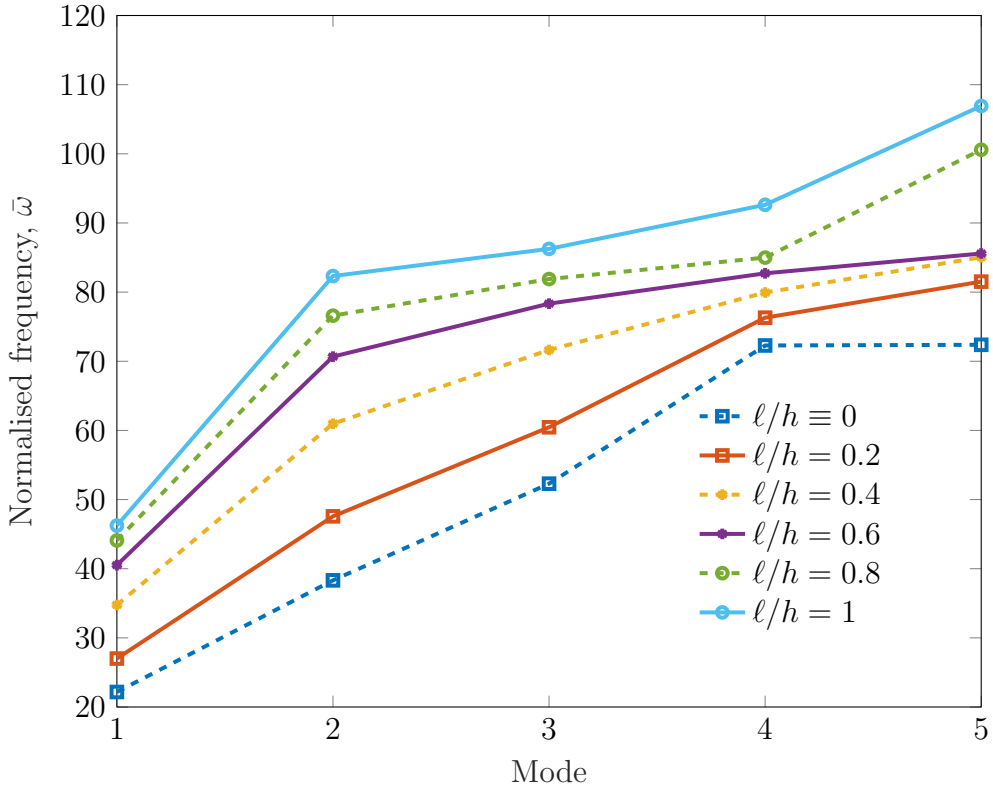

(b) Clamped plate

Figure 8: Effects of material length scale ratio ℓ/h on the natural frequencies of Al/Al_2O_3 square plates with center crack ($a/h = 20$, $c/a = 0.5$, $n = 1$).

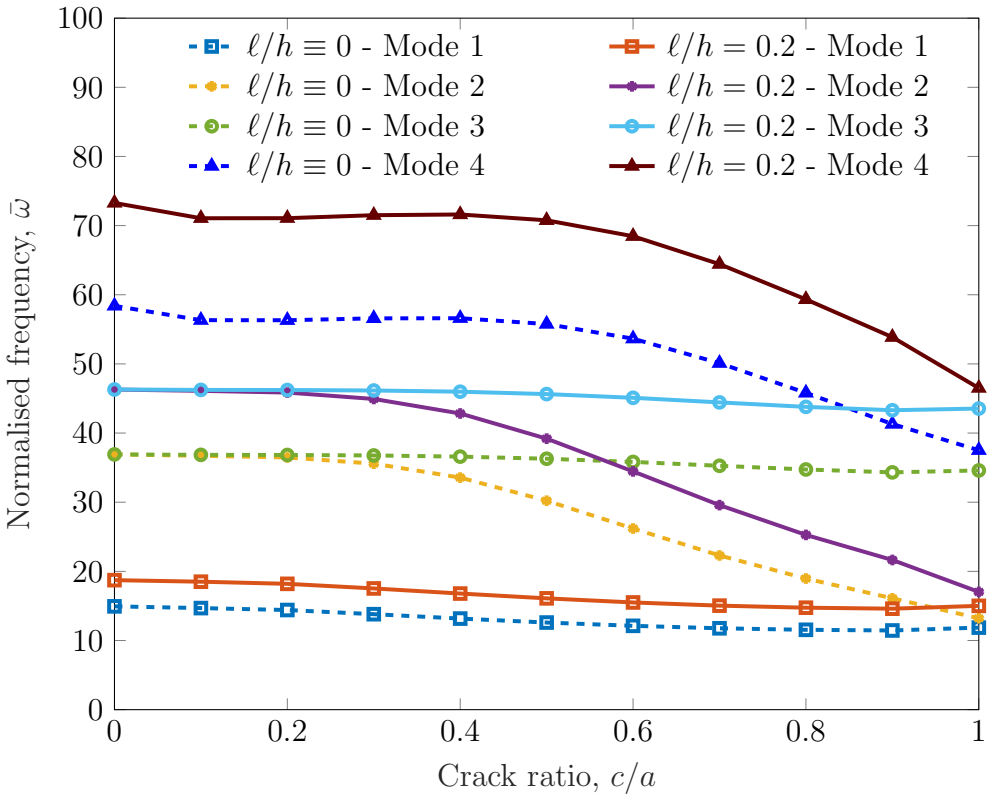

Figure 9: Effects of center crack ratio c/a and material length scale ratio ℓ/h on the frequencies of SSSS Al/Al_2O_3 square plates with center crack, ($a/h = 20$, $n = 1$).

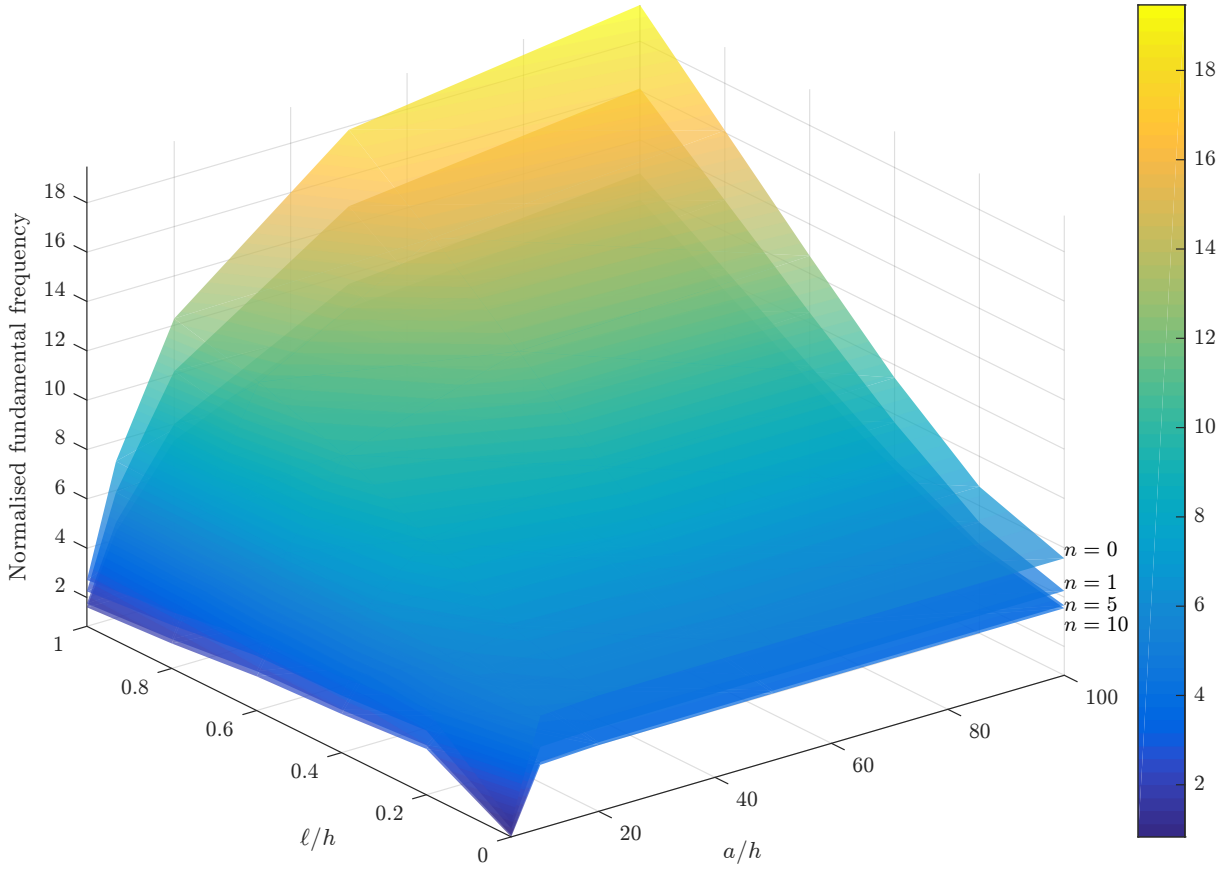

Figure 10: Effects of $\ell/h, a/h, n$ on the fundamental frequencies of SSSS Al/Al_2O_3 square plates with an edge crack, $(c/a = 0.5)$.

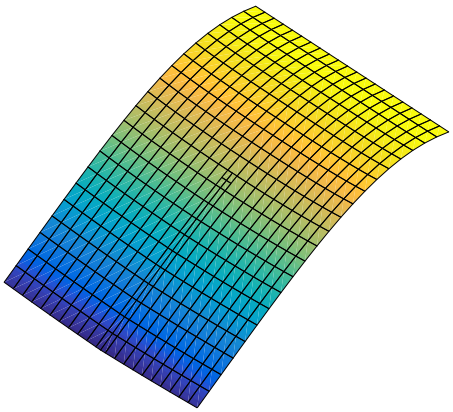

(a) Mode 1

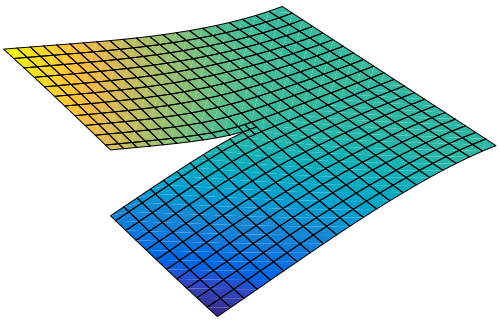

(b) Mode 2

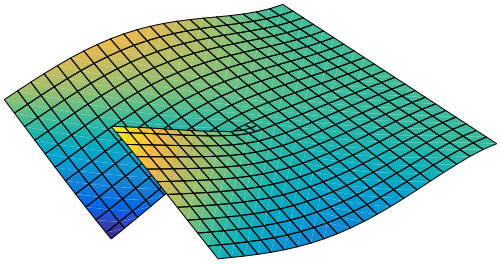

(c) Mode 3

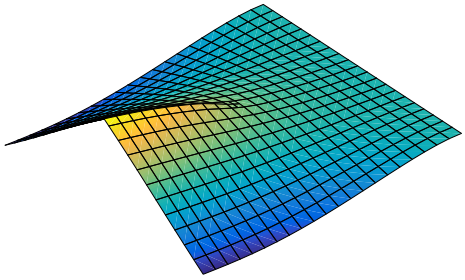

(d) Mode 4

Figure 11: The first four mode shapes of clamped-free Al/Al_2O_3 with an edge crack.

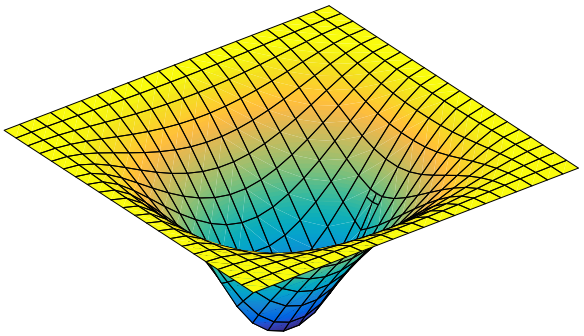

(a) Mode 1

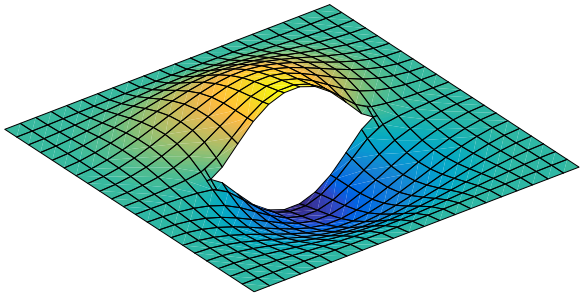

(b) Mode 2

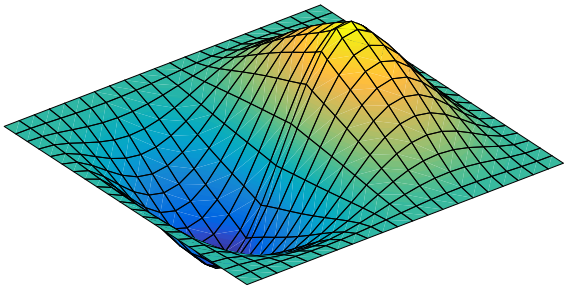

(c) Mode 3

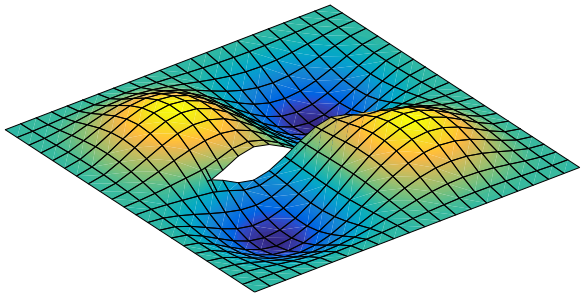

(d) Mode 4

Figure 12: The first four mode shapes of clamped Al/Al_2O_3 with a center crack.

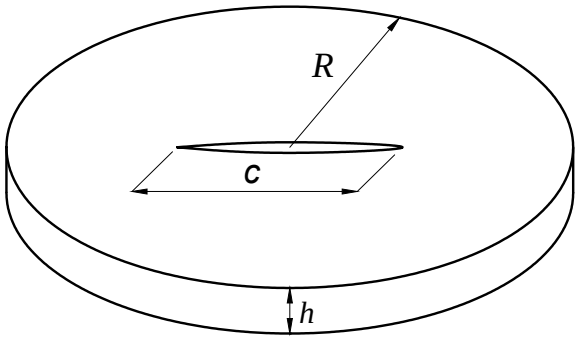

(a) Circular plate

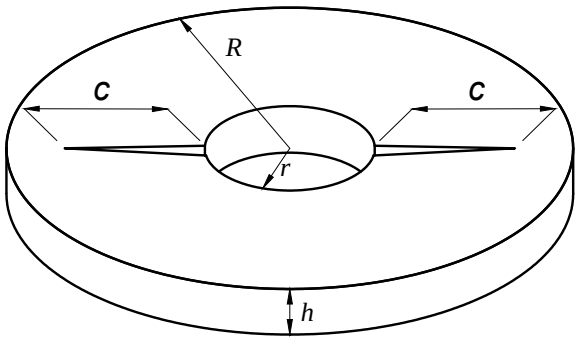

(b) Annular plate

Figure 13: Geometry of circular and annular plates with center cracks.

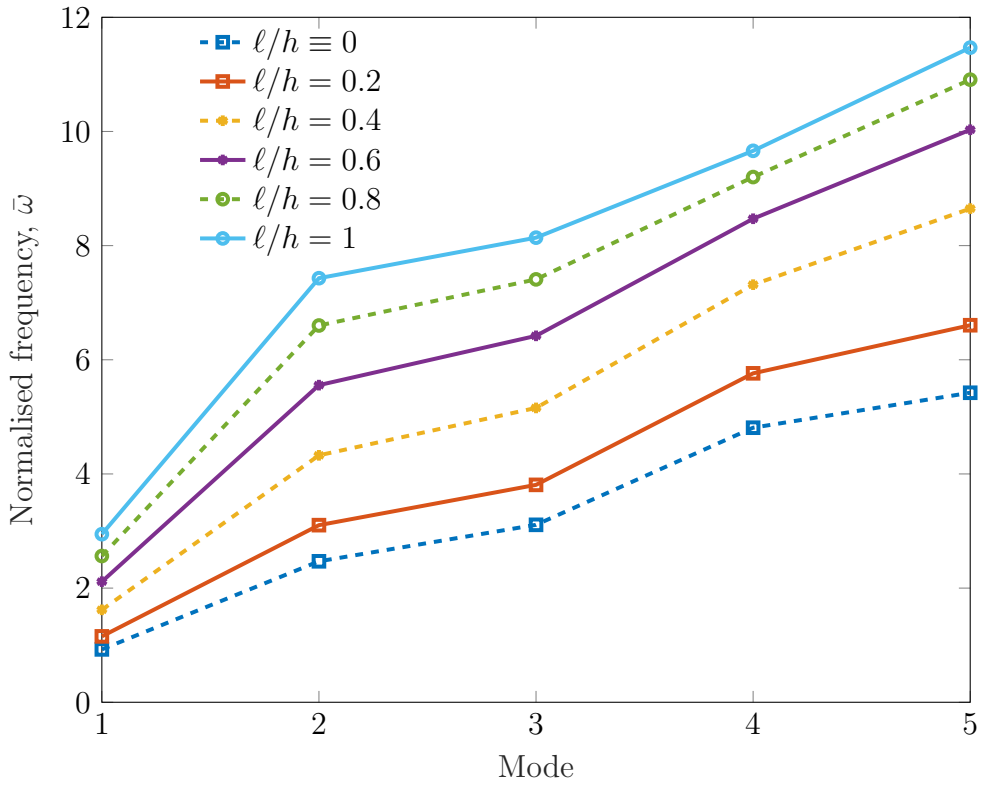

Figure 14: Effects of material length scale ratio ℓ/h on the natural frequencies of simply-supported Al/Al_2O_3 circular plates with center crack, ($h/R = 0.05$, $c/R = 1$, $n = 1$).

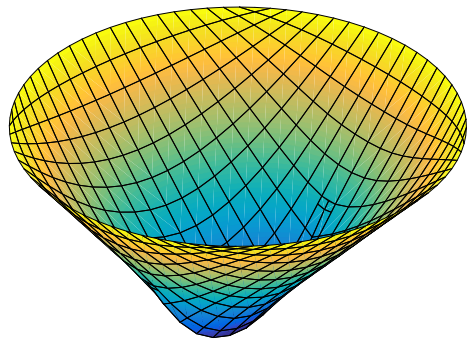

(a) Mode 1

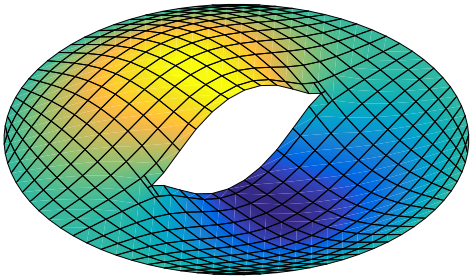

(b) Mode 2

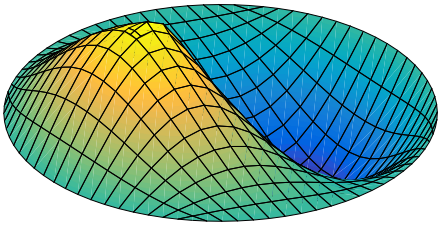

(c) Mode 3

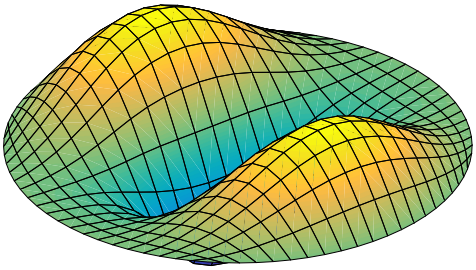

(d) Mode 4

Figure 15: The first four mode shapes of simply-supported Al/Al_2O_3 circular with a center crack.

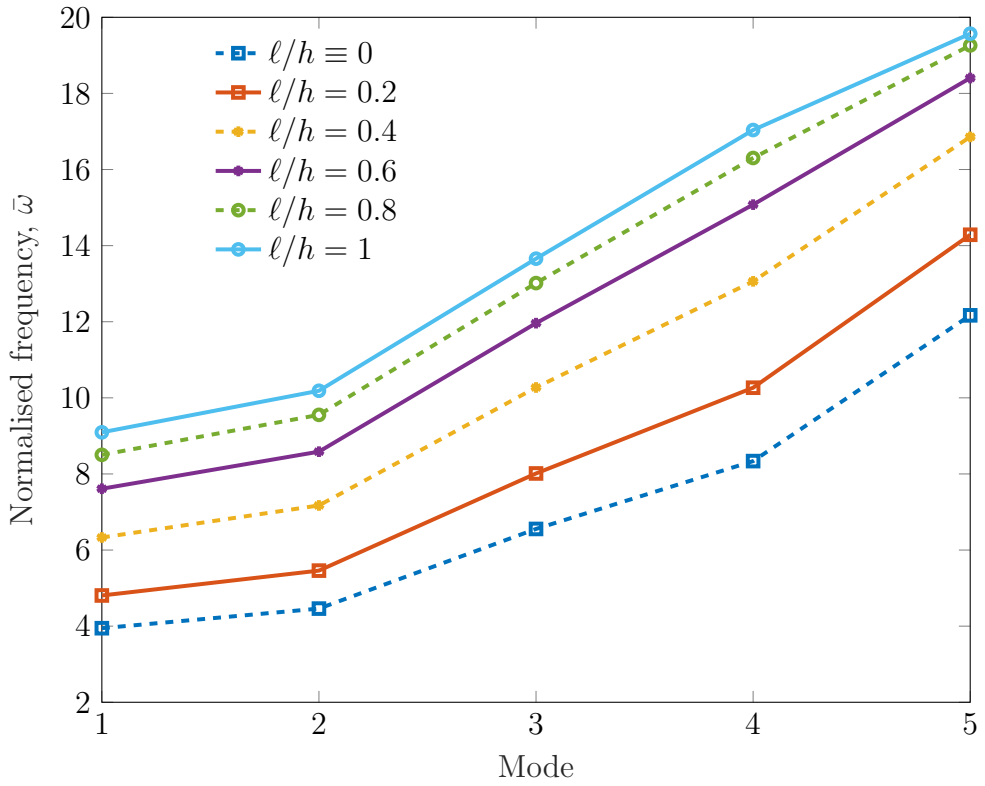

Figure 16: Effects of material length scale ratio ℓ/h on the natural frequencies of Al/Al_2O_3 annular plates with center crack ($h/R = 0.05$, $r/R = 0.5$, $c/(R-r) = 0.5$, $n = 1$).

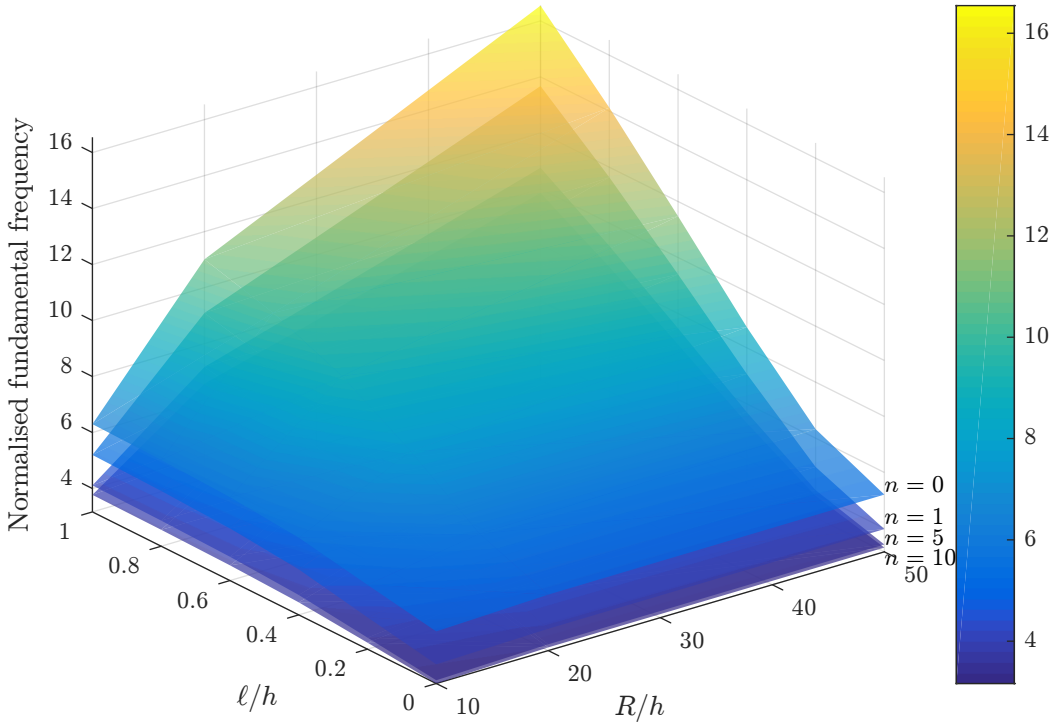

Figure 17: Effects of $\ell/h, R/h, n$ on the fundamental frequencies of Al/Al_2O_3 annular plates with center crack ($c/a = 0.5(R - r)$).

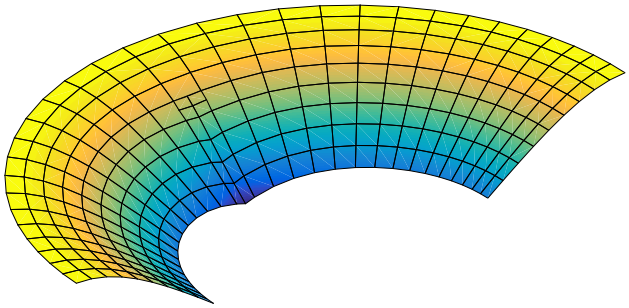

(a) Mode 1

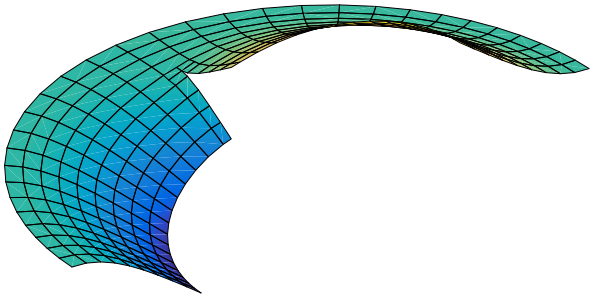

(b) Mode 2

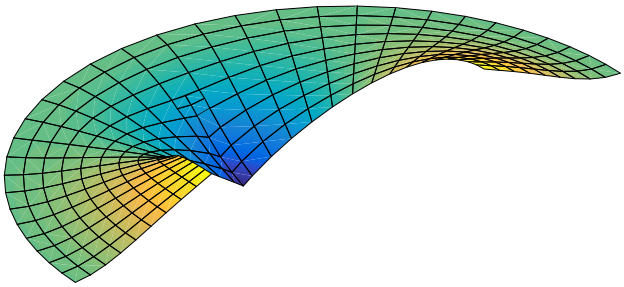

(c) Mode 3

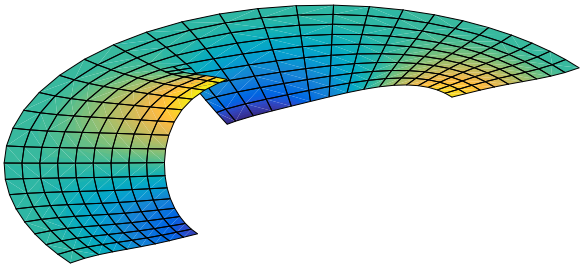

(d) Mode 4

Figure 18: The first four mode shapes of clamped-free a Al/Al_2O_3 half annular plate.